International Journal of Mechanical Sciences 303 (2025) 110614

Contents lists available at ScienceDirect

International Journal of Mechanical Sciences

journal homepage: www.elsevier.com/locate/ijmecsci

Negative stiffness mechanical metamaterial with controllably programmable bandgaps

Wenyou Zha [a], Rui Yang [a], Yongtao Yao [a,*], Yanju Liu [b,c], Jinsong Leng [a,*]

[a] *Center for Composite Materials and Structure, Harbin Institute of Technology, Harbin 150001, PR China*
[b] *Department of Astronautical Science and Mechanics, Harbin Institute of Technology, Harbin 150001, PR China*
[c] *Suzhou Research Institute, Harbin Institute of Technology, Suzhou 215100, PR China*

ARTICLE INFO

Keywords:
Mechanical metamaterial
Vibration isolation
Shape memory
Negative stiffness
Programmable bandgap
Mechanical pixels

ABSTRACT

Materials with wide bandgap distributions have significant potential in the development of novel vibration isolation and damping systems, especially for aerospace and automotive applications. Three mechanical metamaterials were proposed, consisting of negative stiffness elements, honeycomb structures, and resonators, with the negative stiffness elements fabricated from shape memory polymers. By integrating the tunability of smart materials and analyzing from the perspective of phononic crystals, the metamaterials exhibit programmable and highly tunable bandgap properties. The results show that the configuration of negative stiffness elements directly affects the equivalent stiffness of the metamaterial, thereby altering its dispersion relation and transmission properties. The impact of geometric parameters on the modulation of bandgap frequency and transmission properties is systematically verified. Furthermore, two reversible methods, shape memory shape programming and stiffness programming are proposed. The highly nonlinear and impedance mismatch characteristics of the programming structures enable bandgap adjustment under complex loading conditions, achieving full-band vibration isolation within the 1000 Hz frequency range. Additionally, interfaces with different gradients can accurately control the transmission and blocking of excitation frequencies. Programmable coordination based on mechanical pixels ensures the integration of negative stiffness mechanical metamaterials in high precision devices.

1. Introduction

Metamaterials are a class of periodic structures intentionally designed to achieve specific mechanical and physical properties[1]. The mechanical response and fluctuation state of a metamaterial are governed by its unit shape, dimensional parameters, arrangement, and the basic materials used[2,3]. Due to the high degree of design flexibility, metamaterials exhibit tunable properties across various domains[4–7]. This tunability enables the manifestation of unique physical phenomena, such as negative refractive indices and optical invisibility in electromagnetism[8,9], acoustic black holes and localized resonances in acoustics[10,11], negative thermal expansion in thermodynamics[12], as well as negative Poisson's ratios and negative stiffness (NS) in mechanics[13–17]. Additionally, phenomena such as topological mechanical phases[18] and other extraordinary properties are observed. These characteristics have led to the widespread application of metamaterials in fields like wireless communications[19], acoustic control[20,21], energy harvesting and conversion[22], and mechanical control[23].

Due to practical engineering needs, Mechanical metamaterial (MM) is required to serve as support components that can withstand complex loads[24,25]. However, as connecting components, it is difficult to avoid the transmission of vibration induced elastic waves, which must be blocked and attenuated[26–29]. MM with bandgap characteristics can prevent the propagation of elastic waves within certain forbidden frequency ranges[30,31]. The formation of these elastic wave bandgaps typically relies on the resonance effect, structural coupling, and nonlinear effects of periodic units[32–37]. The bionic structures inspired by the natural biological organism structure and function, drawing on their excellent mechanical properties, adaptive capabilities, and multifunctional characteristics, can achieve improvements in structural performance and multifunctional integration[38–43]. Chiral units, due to their unique compression-torsion coupling effect, enable the conversion between longitudinal waves and torsional waves, exhibiting abnormal wave control effects[44–46]. In addition, X-shaped

---

* Corresponding authors.
E-mail addresses: yaoyt@hit.edu.cn (Y. Yao), lengjs@hit.edu.cn (J. Leng).

https://doi.org/10.1016/j.ijmecsci.2025.110614
Received 14 April 2025; Received in revised form 15 July 2025; Accepted 16 July 2025

structures[47–50], plate-like structures[51,52], and self-similar structures[53,54] also exhibit interesting mechanical properties and elastic wave control effects. Origami and its derived structures can achieve multi-modal transformation based on specific mountain-valley line designs or kinematic mechanisms, thereby exhibiting different multi-directional mechanical properties and customized wave propagation paths[55–57]. The liquid-structure coupling in cavity structures [58–60] and gas-structure coupling[61] are also considered effective methods for controlling bandgaps, enabling bandgap control under dynamic conditions without relying on the initial configuration. Piezoelectric active metamaterials based on resonant circuits have been proven to achieve programmable bandgap regulation, and even possess adaptive adjustment capabilities, making them an effective means of dynamically adjusting elastic wave propagation[62–64].

NS elements play a crucial role in energy storage and bandgap formation due to the nonlinear dynamics of elastic buckling instability[65]. The instability of NS elements can be leveraged to produce controllable and reconfigurable morphological changes within the structure, enabling programmed regulation of the bandgap[66]. By combining NS elements with mass concentrating components, a mass mismatch effect can be induced, generating resonance phenomena that open a low frequency bandgap and further expand the overall bandgap range [67,68]. Mass concentrating elements can be fabricated using higher density materials or higher density distributions. NS effects can be generated through springs, flexural beams, and specially arranged magnets[69], Compression can effectively achieve controlled local deformation, influencing bandgap distribution and the evolution of effective bandgap width in various directions[70]. Stress variations within the NS element can significantly affect vibration, leading to symmetric and antisymmetric displacements that contribute to the formation of a low frequency bandgap[66]. The structural damping properties of NS elements provide metamaterials with exceptional acoustic performance, particularly at or above the range of acoustic coincidence[71].

Smart materials can actively adjust their properties in response to changes in the external environment, offering a unique advantage in bandgap regulation[72–76]. By integrating smart materials with metamaterial structures, elastic wave bandgap modulation can be achieved, thereby enhancing the functionality and adaptability of materials in dynamic environments. Metamaterials based on magnetorheological elastomers or magnetorheological fluids have been used to demonstrate multi-directional programmable and reconfigurable bandgaps[73, 77–80], and when combined with origami, they exhibit unexpectedly remarkable performance[81]. The austenitic and martensitic phase transitions of shape memory polymers in response to temperature endow them with programmable and reconfigurable properties without requiring large scale structural or material changes[82]. These materials offer high energy efficiency, overcoming the limitation of irreversible performance after structural molding and significantly expanding the dynamic flexibility of structures. The shape memory behavior of these materials allows for the adjustment of mechanical properties in both spatial and temporal dimensions, enabling programmable elastic wave propagation paths and facilitating active waveguide phenomena [83]. The potential of 4D printing shape memory polymers for designing and fabricating smart devices for elastic wave control and vibration isolation is also highlighted[84,85]. Temperature induced stiffness changes can effectively enhance vibration isolation and reduce resonance frequency [76]. Additionally, Temperature induced transformation of structural configuration effectively broadens the vibration damping range of a structure[86].

In this work, based on thermally stimulated shape memory polymers, three types of bi-material negative stiffness mechanical metamaterials (NSMM) are proposed, combining three types of negative stiffness elements and honeycomb structures made of non-thermo responsive materials. Due to the programmable characteristics of shape memory materials, two reversible programming strategies are proposed to study the evolution of elastic wave bandgaps and vibration responses: shape programming of NSMM and stiffness programming of NS elements in response to temperature. Both experimental and finite element evaluations are conducted. Additionally, the elastic wave propagation behavior under different bandgap gradients is explored through various gradient combinations. The results show that NSMM exhibits different mechanical responses and vibration modes under different forms of negative stiffness elements, and the proposed programming strategies enable full-frequency vibration suppression in the 0-1 kHz frequency range. Furthermore, a vibration control strategy based on lattice mechanical pixels and shape memory polymers is proposed, providing a reliable guide for applying programmable NSMM to space-based on-orbit devices and the automotive industry.

The remaining structure of this paper is as follows: Section 2 details the metamaterial design concept and investigates the fundamental mechanical properties of the required materials. Section 3 evaluates the bandgap evolution and vibration performance of the proposed NSMM programming scheme through experiments and finite element simulations, and develops corresponding analytical models. The elastic wave propagation under different gradient modes is evaluated, and a pixelated vibration control strategy is proposed. Section 4 summarizes several conclusions.

2. Materials and methods

In this section, three novel negative stiffness metamaterials are first proposed, with detailed dimensions specified. Two programming schemes, shape memory shape programming and stiffness programming, based on the thermal programmability of shape memory polymers, are introduced for the dynamic regulation of elastic waves. Subsequently, the process of printing and manufacturing the three metamaterials is described, along with detailed information regarding the testing workflow. Dynamic thermodynamic testing and tensile tests are conducted on standard tensile samples. The relevant setup process for finite element simulations is also introduced.

2.1. *Geometric modeling and Mechanisms*

In this work, NSMM is presented that can be both shape programming and stiffness programming using shape memory smart materials. The structure consists of a mass block, NS element, and rigid honeycomb support structure, with the NS element forming the core of the structure (Fig. 1(a)). The mass block provides mass inertia, influencing the dynamics of the entire structure, while the rigid honeycomb skeleton supports the NS beam, enhancing both the stability of the structure and the effective action range of the NS beams. NS beams are incorporated into the rigid honeycomb and are categorized into three types: slanted beams (S-B), cosine beams (C-B), and folded beams (F-B). The form of these NS beams determines the NS characteristics and vibration isolation properties of the structure. In addition, the NS unit can significantly influence the dispersion relation of the metamaterial, playing a key role in realizing characteristics such as bandgaps and localized modes. After introducing the NS unit, the effective stiffness of the local structure exhibits a non-monotonic or even negative range, thereby inducing new bandgaps or expanding existing ones. The NS units made of shape memory polymers can effectively control the propagation of elastic waves within the programming range. The NSMM is formed by combining the mass block, honeycomb skeleton, and NS beams into a unit, with the resulting structure named S-B NSMM, C-B NSMM, and F-B NSMM, respectively. The cell serves as the foundation for the mechanical properties of the structure. The structure exhibits a high degree of symmetry, which enables effective low frequency modulation of elastic waves. Table 1 gives the dimensional parameters of this work.

The NS beam is fabricated with shape memory smart materials, while the other components are made of non-temperature responsive materials. Shape memory smart materials. Shape memory polymers can adopt temporary shapes under the influence of temperature, and these

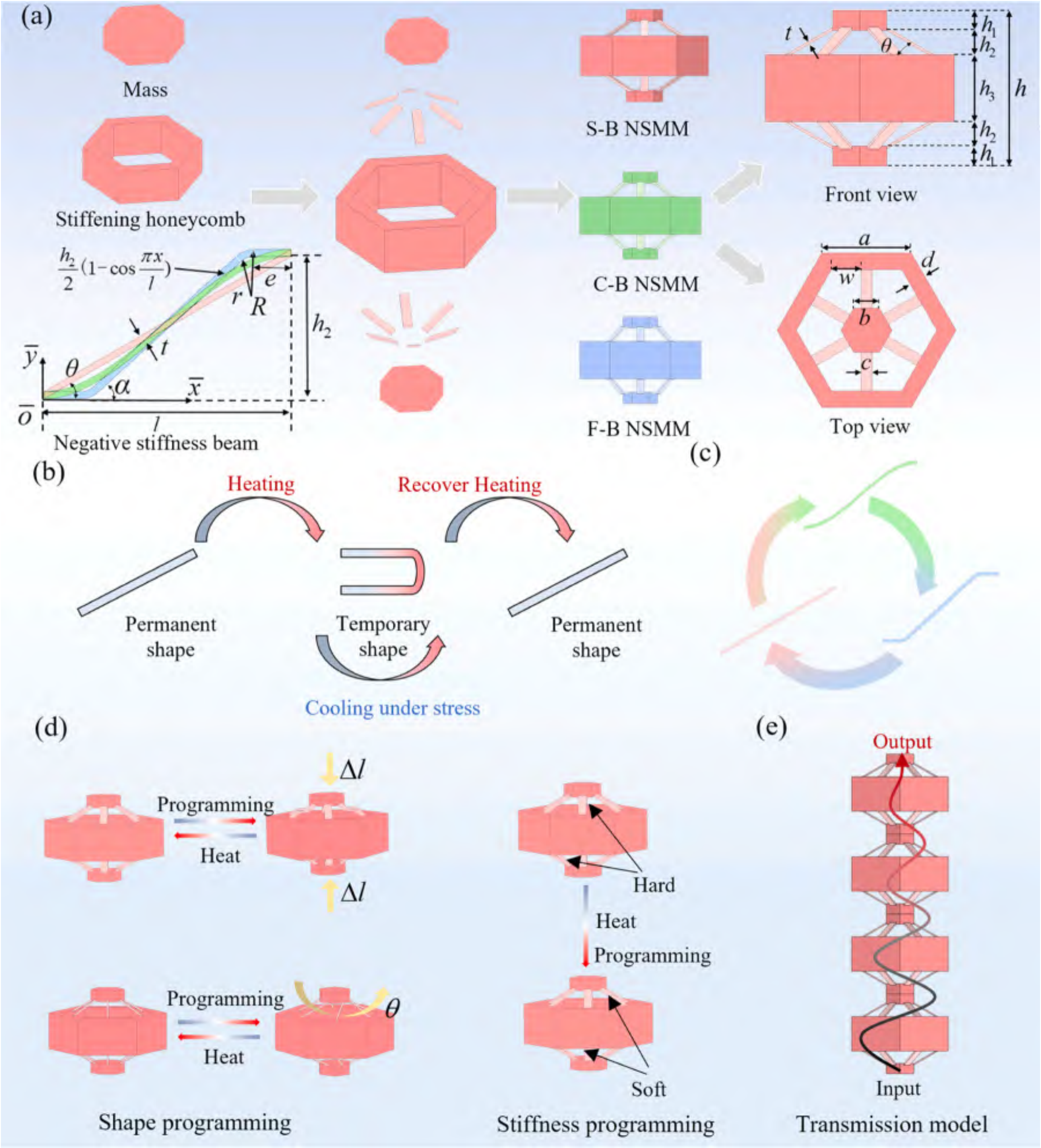

Fig. 1. Design diagram of customizable programmable bandgap NSMM. (a) NSMM element assembly: Consists of a mass block, NS element, and rigid honeycomb wall. (b) Shape memory mechanism. (c) NS element interconversion. (d) Shape memory programming: Shape programming and stiffness programming, are determined by the NS element of the SMP. (e) Transmission model.

shapes can be restored to permanent forms through re-tempering (Fig. 1(b)). Three types of NS beams mutually conform to each other shape by the shape memory effect (Fig. 1(c)). The Fig. A1 provides more details. The programmable transformation of the beams implies that NSMM can also be inter-programmed. Additionally, three programmable strategies are proposed for shape programming and stiffness programming of the beams, based on the programmable properties of the NS elements (Fig. 1(d)). Shape programming includes compression programming and torsion programming, where compression programming alters the nonlinear properties of the beam, and torsion programming affects the height symmetry and nonlinear properties. Stiffness programming, on the other hand, modifies the stiffness of the beam, which is more likely to induce resonance phenomena. The attenuation of elastic waves by NSMM is investigated, with the corresponding elastic wave transmission model shown in Fig. 1(e). The excitation signal used is a sinusoidal excitation per unit acceleration, and the transmission spectrum curves are evaluated for both the excitation and response signals (a_{in} is the excitation acceleration signal, a_{out} is the response acceleration signal, the transmission rate as $T = 20\cdot\log(a_{out}/a_{in})$.).

Table 1
NSMM Dimensional Parameters.

Parameter	Value	Parameter	Value
A	80.83 mm	t	2 mm
B	33.09 mm	θ	30°
C	10 mm	l	45 mm
h_1	15 mm	r	2.22 mm
h_2	17.89mm	R	3.53 mm
h_3	50 mm	w	26.75mm
H	111 mm	e	6 mm
d	15mm	α	45°

2.2. Additive Manufacturing and Mechanical Testing

The CAD model of NSMM was constructed with the help of SpaceClaim, and the material was molded using Bambu Lab P1S fused deposition 3D printing and bonded using a binder. Three key components of NSMM were fabricated using mortise and tenon nesting, molded through fused deposition 3D printing, and subsequently bonded with adhesives to assemble the experimental model (Fig. 2(a)). NS beams were fabricated using shape memory polylactic acid (PLA-SMP), with a terpolymer (ABS) of acrylonitrile (A), butadiene (B), and styrene (S) as the base material for the rigid support and mass oscillator.

The dynamic thermodynamic curves of PLA-SMP were measured by DMA Q800. Mechanical tensile tests were carried out in an Instran 5569 universal electronic testing machine with a temperature box, and the tensile tests were performed according to ASTM D638 with a tensile rate of 2mm/min. For tensile tests at different temperatures, the temperature box was first warmed up to the target temperature, and then the test pieces were kept warm for 15 min and more to ensure that the material was uniformly heated, and then the tensile test was performed subsequently. The tensile standard dog bone was obtained by fused deposition 3D printing. The glass transition temperature (T_g) of PLA-SMP is approximately 67°C, at which the storage modulus decreases and the loss angle increases, peaking at the glass transition temperature (Fig. 2(c)). PLA-SMP exhibits different mechanical responses at varying temperatures (Fig. 2(d)). The mechanical response of ABS was also explored (Fig. 2(e)).

As shown in Fig. 2(b), the variable temperature test, the temperature chamber was adjusted to the target temperature, then the test model was placed into the test chamber, and the bottom of the model was bonded to the fixed plate of the shaker (JZK-10 Shaker), and acceleration sensors (PCB PIEZOTRONICS LW501061) were bonded to the top and bottom of the model, and the temperature was kept constant for 15 min to ensure that the material was uniformly heated, and then the signal was transmitted to the shaker through the signal amplifier (YE5872A), and the signal was captured by the acceleration sensors. (KEYSIGHT 33500B) outputs a sinusoidal swept signal from 0-2000 Hz, which is transmitted to the shaker through a signal amplifier (YE5872A). The signal is captured by the acceleration sensor, acquired and recorded by a signal collector (DH5956), and finally displayed and processed on a computer. Fig. A2 provides more experimental details.

2.3. Finite Element Analysis

The COMSOL solid mechanics module is used to build a finite element model and simulate the structural band gap and transmission spectrum. The Floquet periodic boundary is applied on the bottom surface above and below the mass block and the Brillouin zone is scanned to obtain the structural band gap. Acceleration excitation is applied on the bottom surface to obtain the transfer curve of the structure. Abaqus2021 was employed to analyze load distribution under quasi-static loading. During shape programming, NSMM was compressed at 70°C, followed by bandgap variation analysis at 25°C, with pre-stress effects incorporated.

The geometry of the beam significantly influences the strength and range of the NS response, as well as the overall equivalent stiffness of the metamaterial. These factors, in turn, alter its dispersion relations and bandgap properties. The dispersion curves, transmission spectrum, and vibrational modes of the S-B NSMM are presented in Fig. 3(a). The S-B NSMM exhibits three complete bandgaps in the z direction, corresponding to the frequency ranges of 431.7–977.2 Hz, 1043.9–1298.9 Hz, and 1477.5–2754.9 Hz, where elastic wave propagation is prohibited. The vibrational displacements of the A1 mode is distributed throughout the entire single cell, with deformation energy predominantly concentrated on the inclined beam. This beam is subjected to bending and torsion due to the relatively larger mass and stiffness of the mass block and rigid honeycomb wall. In contrast, the A2 mode exhibits vibrational displacements primarily in the mass block and inclined beam, while the rigid honeycomb wall remains stationary. Similarly, the A3, A4, and A5

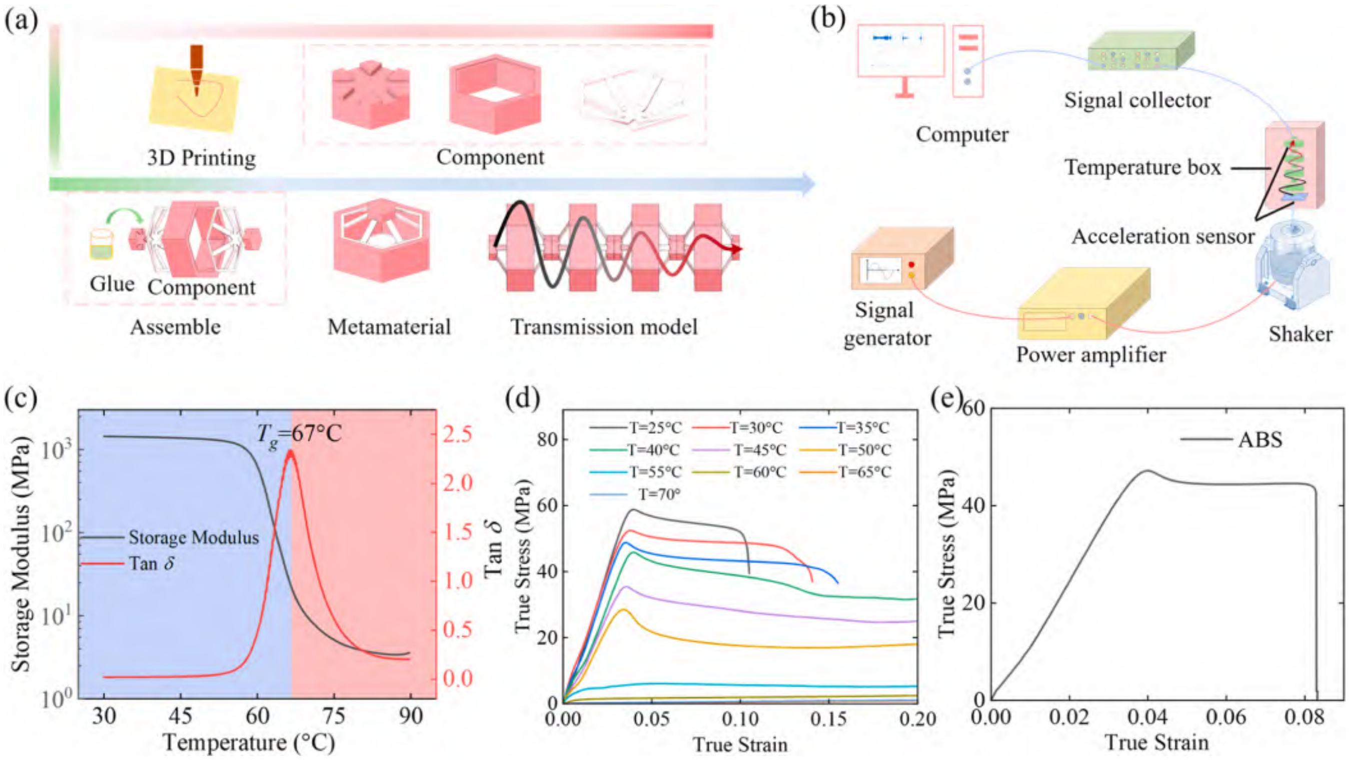

Fig. 2. Additive Manufacturing and Mechanical Testing. (a) Manufacturing and assembly. (b) Experimental vibration test system. (c) Dynamic mechanical properties of PLA-SMP. (d) Mechanical property of PLA-SMP. (e) Mechanical property of ABS. The mechanical property test results will be used for subsequent finite element modeling and simulation analysis.

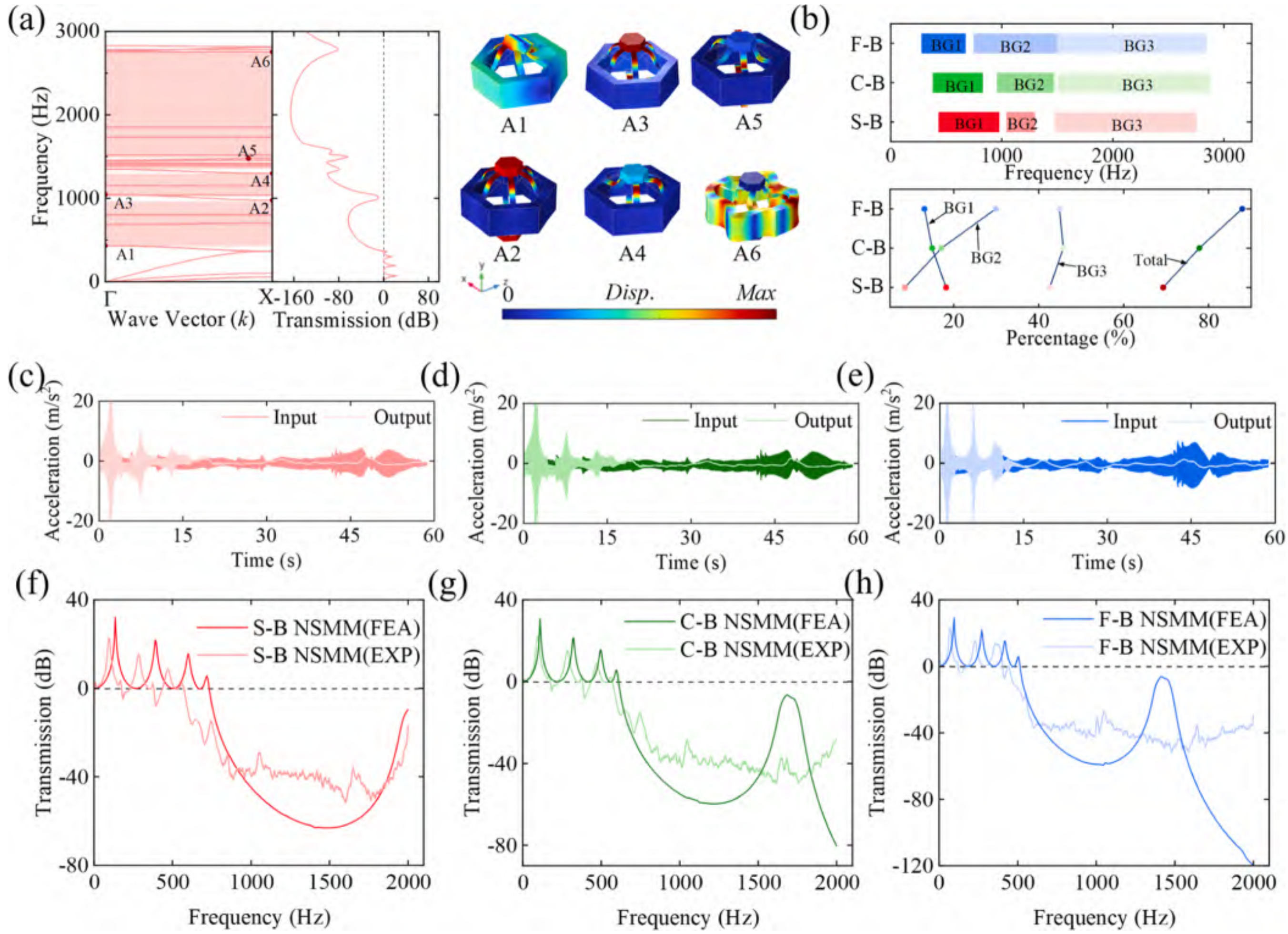

Fig. 3. Bandgap evolution and experimental analysis of NSMM. (a) Transmission spectrum and vibration modes of the S-B NSMM. (b) Bandgap distribution of NSMM. (c) Time domain response of S-B NSMM, (d) C-B NSMM, and (e) F-B NSMM under experimental, vibration signals outside the bandgap are amplified, while those within the bandgap are suppressed. (f) Frequency domain response of S-B NSMM, (g) C-B NSMM, and (h) F-B NSMM under experimental and simulation. The finite element results show good agreement with the experimental results, and the F-B NSMM exhibits superior vibration performance.

modes, demonstrate similar deformation patterns to the A2 mode. The A6 mode, situated at the cutoff frequency of the third bandgap, exhibits an overall deformation pattern across the structure. The dispersion curves and vibrational modes of the C-B NSMM and F-B NSMM exhibit comparable characteristics (Fig. B1). In both cases, the deformation energies are concentrated within the NS beams. The center frequencies of the three bandgaps in the C-B NSMM remain within the same order of magnitude, indicating that the bandgaps are achieved at sub-wavelength dimensions.

Fig. 3(b) illustrates the bandgap distribution and bandwidth share of NSMM. The first bandgap onset frequencies for the S-B, C-B, and F-B NSMM are 431.7 Hz, 380.7 Hz, and 280.6 Hz, respectively. The third bandgap cutoff frequencies are 2754.9 Hz, 2773.5 Hz, and 2848.4 Hz, respectively. The first bandgap intervals are 18.2%, 14.9%, and 13.1%, while the total bandgap intervals account for 69.3%, 77.8%, and 87.9%, respectively. Among the three configurations, the S-B NSMM features the widest first bandgap bandwidth at 431.7 Hz, with a corresponding ratio of 18.2%. On the other hand, the F-B NSMM demonstrates the lowest first bandgap onset frequency (280.6 Hz), the highest third bandgap cutoff frequency (2848.4 Hz), and the largest total bandgap interval, accounting for 87.9%, thereby exhibiting the broadest elastic wave forbidden band.

Fig. 3(c)-(e) shows the time domain response signals of NSMM tested at 25°C. At the initial stage of the applied vibration excitation, the output acceleration significantly exceeds the input acceleration, indicating that the vibration is amplified in the low frequency band. At high frequencies, the input acceleration varies continuously and the output acceleration tends to zero, indicating that the vibration is effectively attenuated. Fig. 3(f)-(h) shows the transmission spectrum of NSMM tested at 25°C, and the transfer curves accurately capture multiple resonance peaks of the structure. The onset frequencies of the damping intervals of NSMM are 571 Hz, 566 Hz, and 440 Hz, respectively, and the transfer curves of the C-B NSMM and the F-B NSMM show a similar trend of change. The F-B NSMM has a lower onset frequency and a wider vibration isolation interval.

The global characteristics of low-frequency vibrations and the local responses of high-frequency vibrations caused the differences between the experimental and finite element results. This is because 3D printing involves layer-by-layer printing, and under an optical microscope, it appears as multiple layers stacked together, with gaps between layers. Additionally, the NSMM is assembled from various components, whereas the finite element model is a perfectly homogeneous model. In the low-frequency range, the vibration modes are relatively simple, primarily reflecting the response of overall stiffness and mass characteristics. The finite element analysis captures these global characteristics more accurately. High-frequency vibrations, on the other hand, usually involve more complex local responses, influenced by factors such as microstructure and local boundary conditions. These factors are not considered in the finite element model, leading to deviations in the high-frequency range. The low frequency vibration transmission spectrum of

NSMM obtained through finite element analysis exhibit the same trend of variation as those from experimental methods and effectively capture the resonance peaks of the structure. In summary, there is good agreement between the finite element model and the experimental structure.

3. Results and discussion

In this section, the dispersion curves, frequency response characteristics, and vibration modes of the three proposed NSMMs are first investigated, and the experimental results are verified with finite element analysis results. The influence of two important geometric parameters on the band gap in specific intervals is discussed. Subsequently, the band gap evolution under shape programming and stiffness programming is explored, and multi-gradient modes are also discussed. Finally, based on the previous research, a vibration control strategy based on lattice mechanics pixels is proposed.

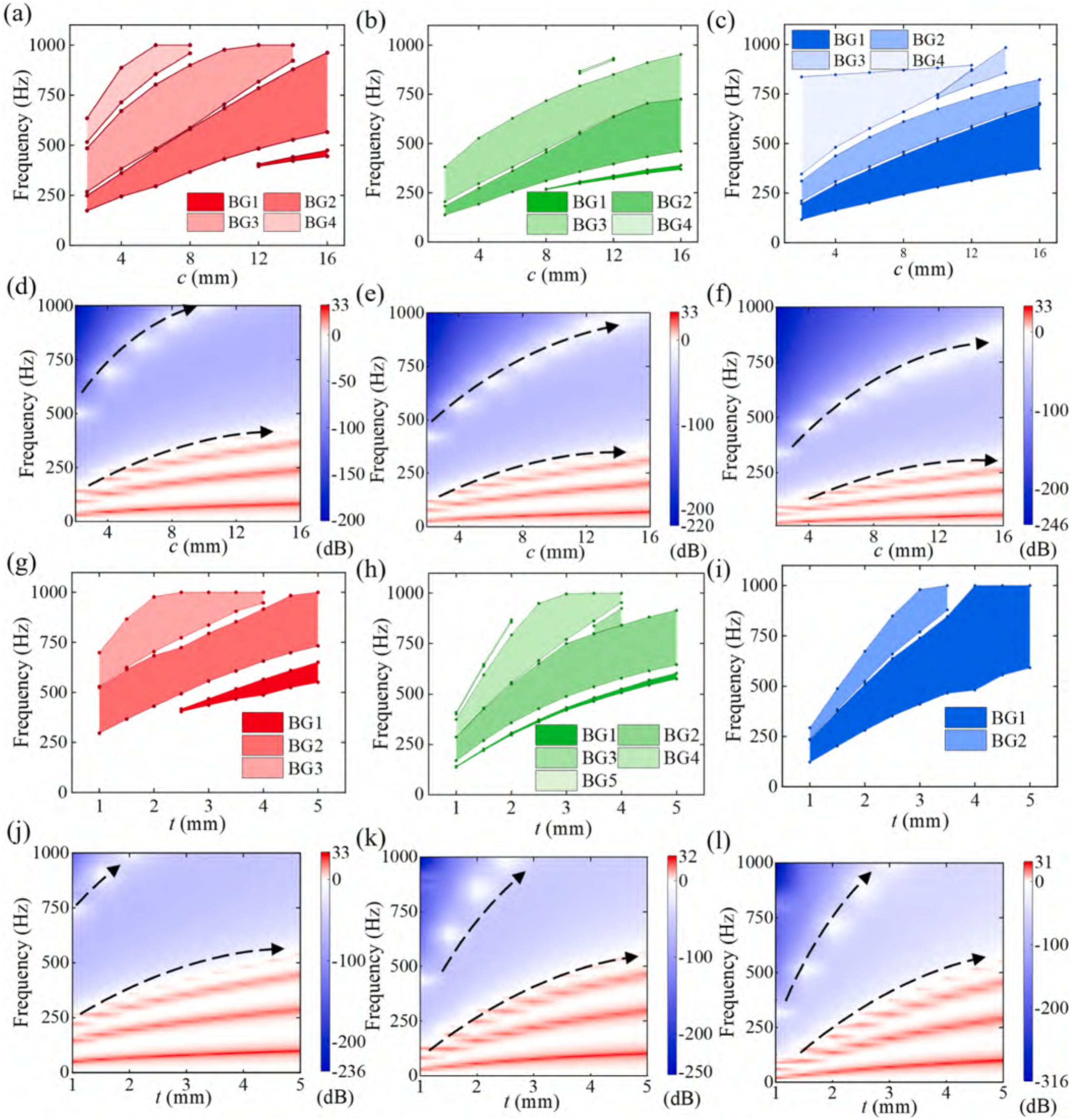

Fig. 4. Bandgap evolution under the Size effect of NSMM. (a) Bandgap evolution of S-B NSMM, (b) C-B NSMM, and (c) F-B NSMM at different widths. (d) Transmission spectrum of S-B NSMM, (e) C-B NSMM, and (f) F-B NSMM at different widths. (g) Bandgap evolution of S-B NSMM, (h) C-B NSMM, and (i) F-B NSMM at different thicknesses. (j) Transmission spectrum of S-B NSMM, (k) C-B NSMM, and (l) F-B NSMM at different thicknesses. The trends of bandgap evolution and transmission variation under the influence of geometric parameters are consistent.

3.1. Bandgap evolution under the influence of NSMM dimensions

The dimensional parameters of the structure play a critical role in determining the bandgap distribution and elastic wave transmission. Width and thickness are two key parameters that influence the NS beams. An increase in beam width enhances the effective stiffness of the NS beam, which raises the intrinsic frequency of the vibrating system, thereby increasing both the boundary frequency and bandwidth of the bandgap.

Fig. 4(a)-(c) shows the evolution of the bandgap for NSMM, where the onset frequency of the bandgap boundary gradually increases with increasing width, and the bandgap width increases monotonically. The increase in width results in the opening and closing of the bandgap. The opening of the bandgap has a particularly significant effect on the low frequency bandgap. At lower widths, the reduced beam stiffness enhances coupling with the mass block, leading to stronger resonance phenomena and greater energy dissipation. This manifests as an increase in elastic wave transmission (Fig. 4(d)-(f)). The cosine beam exhibits stronger geometric nonlinearity and can open the first bandgap (BG1) earlier than the inclined beam at the same width. Fig. 4(d)-(f) displays the transmission spectrum of the three NSMM, along with the variation of the width c, which also shows white bands connecting regions that correspond with the bandwidths and cutoff frequencies of the respective wide bandgaps. At lower widths, the blue band starts at a lower frequency and experiences less transmission at the same frequency. A smaller width reduces the effective stiffness of the beam, making it more prone to resonance with the mass block, which increases energy dissipation. The F-B NSMM has the widest bandgap and exhibits better elastic wave attenuation across successive variations of width c, as well as a lower onset frequency.

The thickness of the NS beam is a critical parameter in determining the effective stiffness of the beam. Fig. 4(g)-(i) illustrates the structural energy bandgap evolution of the NS beams under the influence of successive 1-5 mm variations in thickness while keeping the other dimensions of NSMM constant. The overall bandgap distribution of the S-B NSMM influenced by thickness is similar to that of the ligament width effect. However, increasing thickness results in a more pronounced opening of the low frequency bandgap (BG1). As the thickness increases, the center frequency, cutoff frequency, and bandwidth of the bandgap all shift higher. BG2 of the S-B NSMM forms a complete bandgap, and its center frequency increases with thickness. The bandgap of the S-B NSMM is fully developed because the effective stiffness of the NS beam increases with increasing thickness, causing the overall bandgap range to shift toward higher frequencies.

The high frequency bandgap of the C-B NSMM is significantly affected by thickness changes, with some bandgaps (BG4 and BG5) closing due to the increase in thickness. The increase in thickness has an even more pronounced effect on the high frequency bandgap of the F-B NSMM, indicating that the folded beam design offers greater bandgap regulation in the high frequency range. Fig. 4(j)-(l) displays the transmission spectrum of the three NSMM at different ligament thicknesses. Similar to the transmission results for the width parameter, the blue band in the middle of the white band corresponds to the bandgap width and cutoff frequency at the respective dimensions, with good agreement.

The cases of low thickness and low width exhibit similar behavior, as the reduced effective stiffness of the ligaments leads to more resonance with the mass block, resulting in significant dissipation of low frequency vibrational energy. This behavior is more favorable for opening the low frequency bandgap, with the blue bands showing lower onset frequencies. As the thickness increases, the effective stiffness of the NS beams rises, and the transmission shifts to higher frequencies. The F-B NSMM shows the widest bandgap and superior elastic wave attenuation under continuous thickness variation, with lower cutoff frequency boundaries, demonstrating significant low frequency vibration isolation capability. After an increase in thickness, the high frequency bandgap and transmission loss performance of the F-B NSMM surpasses that of the S-B and C-B NSMM.

3.2. Programmable Shape Response

Metamaterial structures used in engineering applications must endure complex loads. A single configuration is insufficient to block and absorb the vibration energy generated by such loads. To address this, shape memory programming is employed to induce changes in ligament configurations, enabling the evolution of the bandgap and the realization of adjustable bandgap characteristics. Two programming schemes are proposed: compression programming (Fig. 5(a)) and torsion programming (Fig. 5(f)). Fig. A3 shows the corresponding shape programming.

In the shape programming scheme, NSMM programming focuses on the NS beam, which maintains its shape and then transmits vibrations. Fig. C1 shows the quasi-static compression simulations of NSMM with different ligament parameters. The deformation process is divided into three stages: Stage 1 (positive stiffness, elastic deformation), Stage 2 (NS, elastic destabilization deformation), and Stage 3 (positive stiffness, plastic deformation in the dense stage). The compression mechanics curves of the S-B NSMM show that the peak values gradually increase with the width and thickness of the ligaments, enhancing the NS characteristics and energy absorption capacity. Specifically, the width change does not affect the zero potential energy point. The initial stiffness of the C-B NSMM is lower than that of the S-B NSMM, but the NS stage starts earlier, suggesting that the geometric design of the cosine beams is more prone to destabilization. The initial stiffness of the F-B NSMM is the lowest, indicating that the folded beams are more susceptible to bending deformation.

Fig. 5(c)-(e) shows the bandgap evolution of NSMM under shape programming while Fig. C2 provides more detailed bandgap distributions and elastic wave transmission evolution of S-B NSMM. Compared to the initial configuration, the programming NSMM opens up the low frequency bandgap, shifts the first bandgap downward, and narrows the bandwidth, resulting in a lower onset frequency. This shift is due to the significant reduction in the effective stiffness of the programming NSMM, which, according to the single degree of freedom mass spring vibration system, lowers the intrinsic frequency and the cutoff frequency of the bandgap. Compression programming enhances the nonlinear effects of the structure and induces local resonance phenomena in the NS section, further opening up additional bandgaps. The NS property also increases the impedance mismatch region of the structure, resulting in a broader bandwidth. As the effective stiffness of NSMM decreases due to compression programming, the intrinsic frequency drops, and the impedance mismatch, along with nonlinear mode coupling induced by the stiffness reduction, significantly affects the bandgap evolution. The bandgap distributions of NSMM with varying degrees of programming exhibit multiple energy band branches in the bandgap regions, approximating horizontal straight lines (Fig. C2). In this case, the group velocity is represented by a horizontal straight line with a slope close to zero. Observing NSMM transmission spectrum, compression programming reduces the amount of transmission, while the nonlinear effects of the structure weaken the system damping, increasing transmission loss.

Fig. 5(b) displays NSMM vibration modes at an excitation frequency of 250 Hz. In the initial state, the excitation falls within the passband, allowing the elastic wave to propagate. The NSMM responds with a synergistic displacement deformation of the entire structure. However, when the excitation frequency is within the forbidden band of the programmed NSMM, the elastic wave cannot propagate. The vibrational energy is strongly attenuated within the first single cell, remaining confined to the location of the excitation and failing to induce displacement across the overall structure. This local resonance phenomenon arises from Brillouin scattering and impedance mismatch in the forbidden frequency range, causing the structure to exhibit strong reflective properties at that frequency.

For the torsional programming scheme, NSMM programming focuses

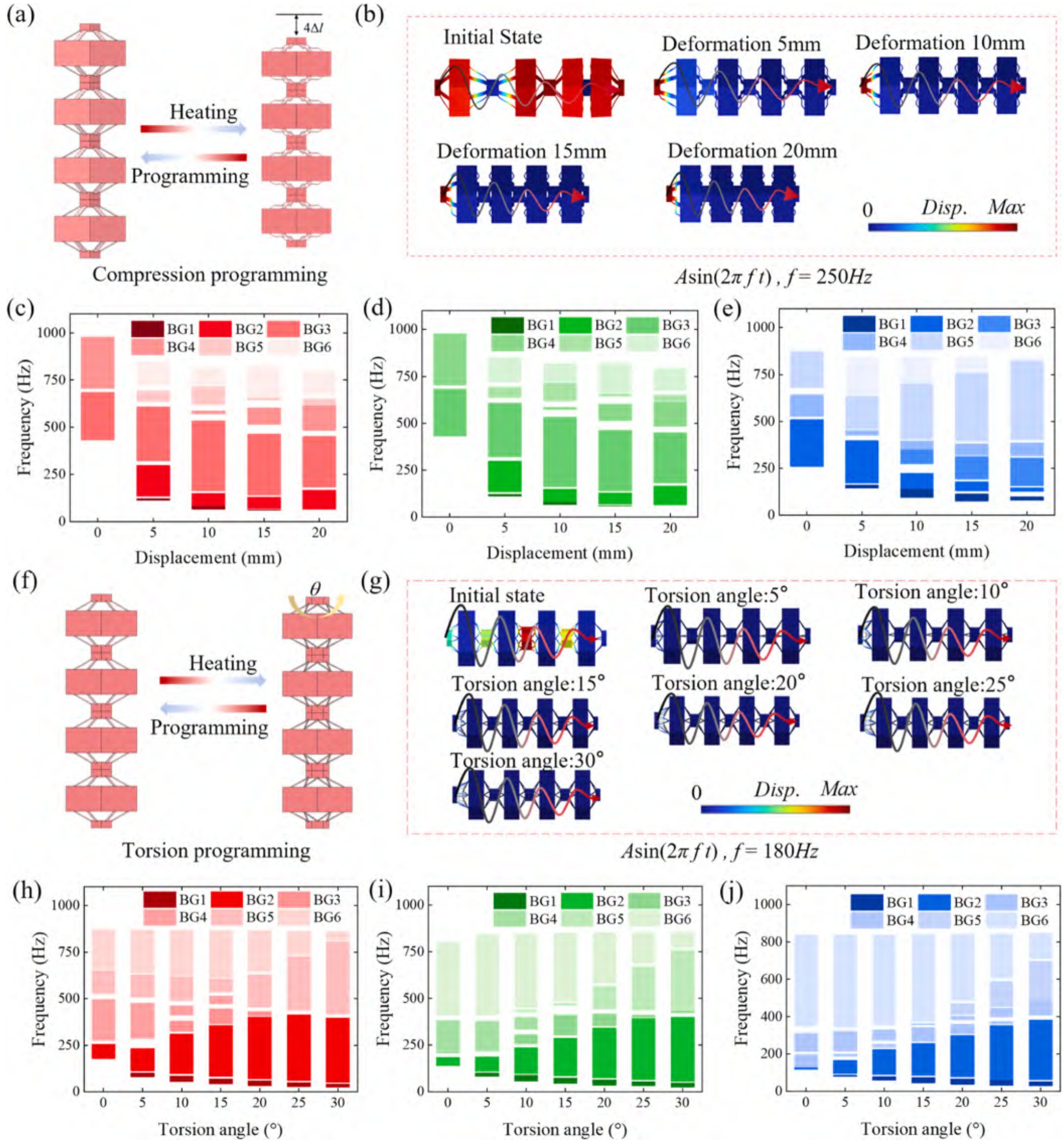

Fig. 5. Programmable shape response and bandgap evolution of NSMM. (a) Schematic and vibrational diagrams of compression shape programming in S-B NSMM. (b) Schematic and vibrational diagrams of torsion shape programming in S-B NSMM. (c) Bandgap evolution of S-B NSMM, (d) C-B NSMM, (e) F-B NSMM under different compression programming states. (f) Bandgap evolution of S-B NSMM, (g) C-B NSMM, (h) F-B NSMM under different torsion programming states.

on the NS beam, which maintains its shape while performing the vibration transfer. The bandgap distributions of the three NSMM at various torsion angles are shown in Fig. 5(h)-(j), and Fig. C3 provides more detailed bandgap distributions and transmission spectrum evolution. The bandgap exhibits significant dynamic changes with the torsion angle, with the number of bandgaps increasing and then decreasing as the torsion progresses. The F-B NSMM, in particular, has a much lower onset frequency in its initial state, and its bandgap distribution is more complex, especially below 300 Hz and above 600 Hz, where significant changes in distribution occur. This indicates that torsional programming intensifies the non-uniformity of the stiffness distribution within the structure. As a result, the mode spacing narrows, higher order modes are activated, and geometrical nonlinear effects coupled with periodic damage enhance modal coupling. These factors lead to a gradual reduction in the passband bandwidth between bandgaps, reflecting the significant modulation of the structural fluctuation characteristics due to torsion. This phenomenon highlights the profound impact of torsional programming on the bandgap characteristics and vibration isolation performance of the NS structures. Additionally, the inherent nonlinear geometry of NSMM further influences the torsional modulation of the elastic wave propagation. The bandgap distributions for NSMM with varying degrees of programming exhibit multiple energy band branches that approximate a horizontal straight line. In this scenario, the group velocities correspond to a horizontal line with a slope close to zero.

Fig. 5(g) shows the vibration displacement distribution at an excitation frequency of 180 Hz for NSMM under torsion programming. In the passband frequency, elastic waves can propagate through the structure, causing overall vibration deformation. However, when the excitation frequency falls within the forbidden band, the elastic waves are strongly attenuated within the excitation unit cell, resulting in only local vibration deformation confined to the excitation cell.

Although the NS elements of the NSMM differ in specific geometric forms, they all possess a certain periodic structure, which similarly modulates the elastic wave propagation characteristics. Additionally, under different torsion angles, the modal distributions of the folded beams and cosine beams are affected by torsion-induced breaking of high symmetry and adjustments to local stiffness, resulting in similar band structure characteristics under these conditions. Compared to S-B NSMM, the geometric complexity of C-B and F-B NSMM is higher, especially in the high-frequency range, where they introduce dense local resonance modes, causing their band gap distributions to converge in the high-frequency region.

3.3. Programmable stiffness response

The beams of NSMM can be interchanged among slanted, cosine, and folded beams due to the shape programmable properties of shape memory smart materials, allowing dynamic regulation of elastic wave transmission and isolation through conformational changes. Additionally, the mechanical properties of NSMM are temperature dependent (Fig. 6(a)), enabling the structural stiffness of PLA-SMP based NS beams to be dynamically adjusted. This adjustment enhances the likelihood of resonance with the mass block and rigid honeycomb wall, overcoming limitations imposed by size and external conditions. This regulation facilitates the intelligent evolution of elastic waves, significantly contributing to vibration control.

Another effective control strategy involves the use of payloads, as shown in Fig. 6(b), where additional mass is employed to achieve vibration suppression. This approach has demonstrated effectiveness and is more aligned with engineering practices. Analogous to a single degree of freedom vibration system, stiffness programming enables precise control of effective stiffness, while the payload influences the mass. Further experimental details are provided in Fig. A2.

The stiffness programming bandgap evolution of NSMM under temperature control (Fig. 6(d)) demonstrates that both bandgaps shift toward lower frequencies as the temperature increases, exhibiting lower onset frequencies and narrower bandwidths. At elevated temperatures, both BG1 and BG2 experience significant narrowing. The temperature sensitivity of the shape memory material is crucial, as it causes a marked reduction in both bending and tensile stiffness with increasing temperature. Like a spring mass oscillator model, the decrease in structural stiffness, with the mass remaining constant, results in a lower intrinsic frequency. Consequently, as the temperature rises, the entire bandgap shifts to lower frequencies, while the density of higher modes increases, further narrowing or even closing the bandgap. Additionally, due to the inherent geometric properties of NSMM, localized vibration modes in the beam become more pronounced at higher temperatures, enhancing the energy confinement effect and increasing transmission in the high frequency range. The trend of the white band, influenced by temperature, aligns with the bandgap evolution observed in Fig. 6(d). The transmission spectrum of NSMM is provided in Fig. C4. As the temperature increases, the blue bands at the same frequency deepen in color for NSMM, indicating an enhanced elastic wave blocking capability. This is because the shape memory material is temperature-sensitive, and the NS beams are made from shape memory materials whose elastic modulus decreases significantly with rising temperature. This leads to a reduction in the structure's bending and tensile stiffness. Analogous to a spring-mass oscillator model, the structural stiffness decreases while the mass remains unchanged, resulting in a lower natural frequency. As the temperature rises, the entire bandgap shifts toward lower frequencies, and the density of higher modes increases, causing the bandgap to narrow or even close. Additionally, due to the geometric characteristics of the NSMM, local vibration modes in the beams become more pronounced at high temperatures, enhancing energy confinement effects and thereby increasing transmission loss in the high-frequency range.

A three mass block double spring system was developed to characterize the variation of NSMM band gap with temperature (Fig. 6(c)). In this model, the NS element of the SMP was represented as a spring, while the mass block and rigid honeycomb wall was modeled as mass blocks. This simplified mechanical system allows for the analysis of the temperature induced changes in the bandgap by simulating the dynamic interactions between the springs and mass blocks under varying thermal conditions.

For three spring and two mass oscillator model, cell i as the characteristic cell, the equation of motion of the mass block, derived from the kinetic equilibrium relationship, is expressed as follows:

$$\begin{cases} m_1\ddot{x}_{2i-1} = f_L - c_T(\dot{x}_{2i-1}-\dot{x}_{2i}) - k_T(x_{2i-1}-x_{2i}) \\ m_2\ddot{x}_{2i} = c_T(\dot{x}_{2i-1}-\dot{x}_{2i}) + k_T(x_{2i-1}-x_{2i}) - c_T(\dot{x}_{2i}-\dot{x}_{2i+1}) - k_T(x_{2i}-x_{2i+1}) \\ m_1\ddot{x}_{2i+1} = c_T(\dot{x}_{2i}-\dot{x}_{2i+1}) + k_T(x_{2i}-x_{2i+1}) - f_R. \end{cases} \tag{1}$$

The system dynamics equations can be obtained by organizing,

$$M\ddot{x} + C\dot{x} + Kx = f, \tag{2}$$

where the displacement vector is $x = [x_{2i-1}, x_{2i}, x_{2i+1}]^T$, the external force vector is $f = [f_L, 0, f_R]^T$.

The mass matrix M, the damping matrix C, and the stiffness matrix K are,

$$M = \begin{bmatrix} m_1 & 0 & 0 \\ 0 & m_2 & 0 \\ 0 & 0 & m_1 \end{bmatrix}, C = \begin{bmatrix} c_T & -c_T & 0 \\ -c_T & 2c_T & -c_T \\ 0 & -c_T & c_T \end{bmatrix}, K = \begin{bmatrix} k_T & -k_T & 0 \\ -k_T & 2k_T & -k_T \\ 0 & -k_T & k_T \end{bmatrix}. \tag{3}$$

Consider the periodic system as a resonant problem, we have:

$$x = Xe^{i\omega t}, f = Fe^{i\omega t}. \tag{4}$$

In practice, material and structural damping are often neglected in bandgap studies, as damping is typically discussed in the context of transmission spectrum. Bringing Eq(4) into Eq(2) and organizing it yields,

$$(K - \omega^2 M)X = F. \tag{5}$$

Based on the Bloch boundary conditions, the following relationship exists between the single cell displacements and boundary forces,

$$X_{2i+1} = X_{2i-1}e^{-iqa}, F_{2i+1} = F_{2i-1}e^{-iqa}. \tag{6}$$

In the above equation, k is the Bloch wave vector and a is the feature length.

Let $X = A\overline{X} = \begin{bmatrix} 1 & 0 \\ 0 & 1 \\ e^{-iqa} & 0 \end{bmatrix} \begin{bmatrix} X_{2i-1} \\ X_{2i+1} \end{bmatrix}$, bring in Eq(5), and multiply left by $\overline{A} = \begin{bmatrix} 1 & 0 & e^{iqa} \\ 0 & 1 & 0 \end{bmatrix}$, which yields,

$$(\overline{K} - \omega^2\overline{M})\overline{X} = 0, \tag{7}$$

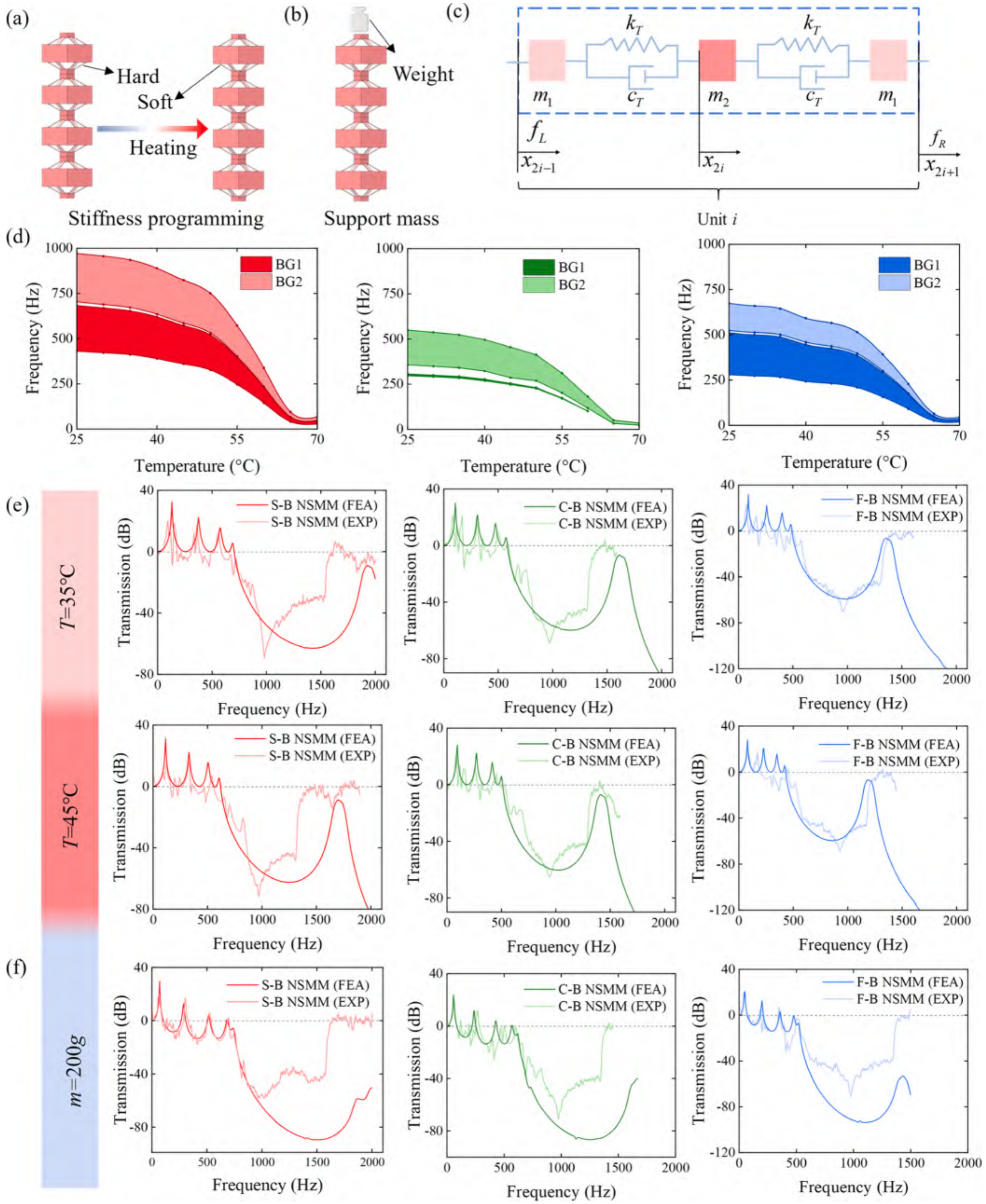

Fig. 6. Programmable stiffness response bandgap evolution of NSMM. (a) Stiffness programming of NSMM, the stiffness of the SMP decreases sharply under high temperature. (b) Payload strategy for vibration suppression using additional mass. (c) Spring mass system model. (d) Bandgap evolution of NSMM as a response to programmable stiffness adjustments. (e) Transmission spectrum evolution of NSMM at different stiffness programming states, comparing experimental and simulation results corresponding to temperature points of 35°C and 45°C. (f) Transmission spectrum of NSMM under a 200 g payload, showing experimental and simulation results for vibration suppression. Both stiffness programming and applied payload can achieve vibration suppression.

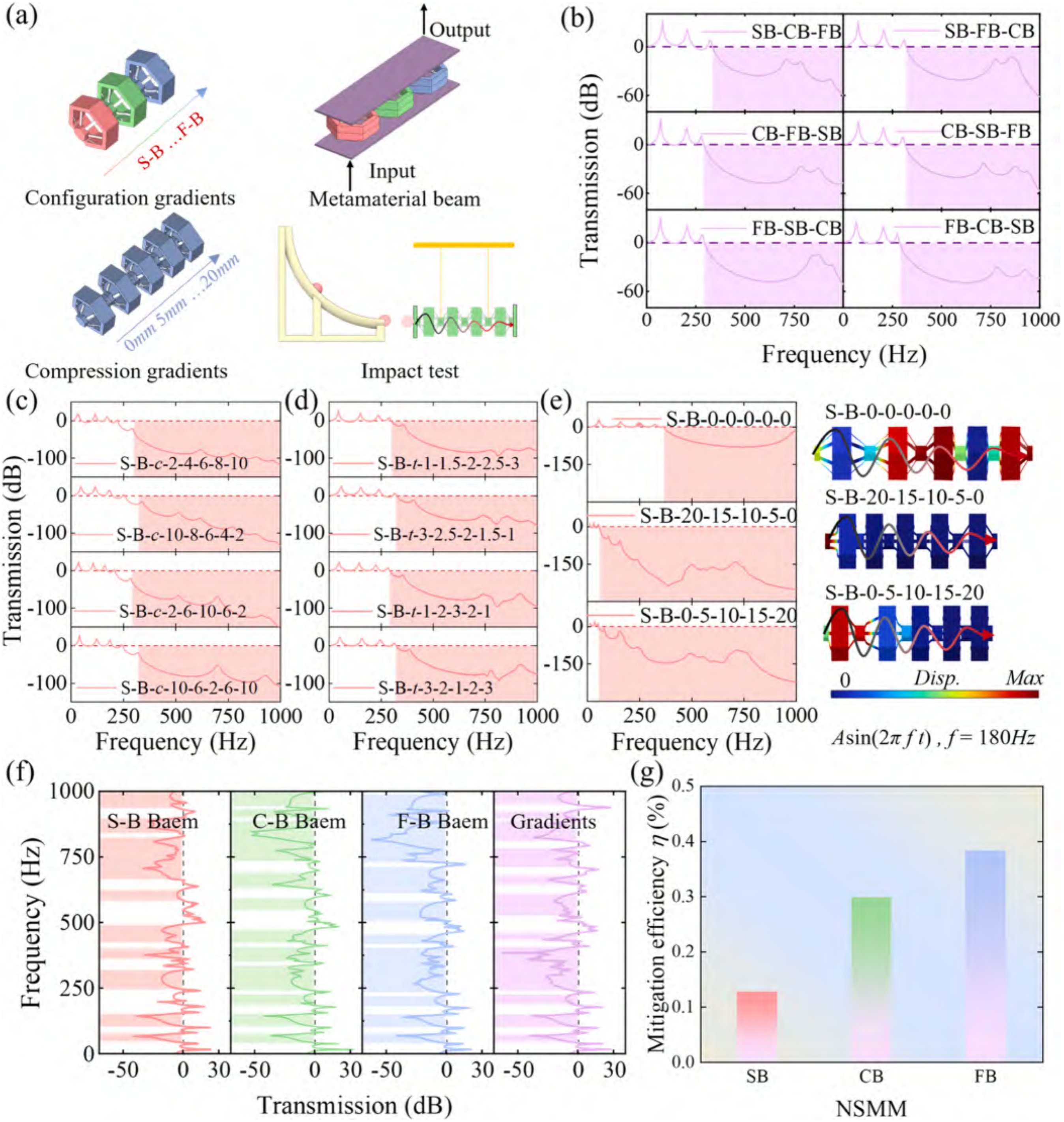

Fig. 7. NSMM Programming Effects and Their Applications. (a) Gradient structure, beam structure, and impact model of NSMM, showcasing programmable structural configurations. (b) Transmission spectrum corresponding to alignment order, highlighting the effect of structural alignment on wave propagation. (c) Compression programming gradient transmission spectrum, illustrating the influence of gradient compression programming on wave transmission. (d) Transmission spectrum of the beam structure, demonstrating the wave propagation characteristics of the programmable beam configurations. (e) Impact mitigation efficiency of NSMM.

where, $\overline{K} = \overline{A}KA$, $\overline{M} = \overline{A}MA$.

Solving to get the eigenvalue problem,

$$\det(\overline{K} - \omega^2\overline{M}) = 0. \tag{8}$$

The solution of the above equation is the corresponding bandgap onset and cutoff frequencies. The equivalent stiffness of NSMM is discussed in Appendix D.

Fig. 6(e) demonstrates the transmission spectrum of NSMM programmed at stiffness levels corresponding to 35°C and 45°C. As the temperature increases, the initial frequency of the damping interval decreases, the effective damping interval narrows, and multiple damping intervals appear in the low frequency band. These changes enhance the vibration isolation performance of the structure. The temperature rise reduces the structural elastic modulus, decreasing the effective stiffness of the structure and consequently lowering the intrinsic frequency. Simultaneously, the increased temperature enhances the damping properties of SMP, further improving the structural vibration isolation capability.

The finite element analysis results align closely with the experimental results, accurately capturing resonance peaks caused by the matching of external excitation frequencies and the system natural frequencies, which lead to vibration amplification. Additionally, both approaches successfully capture the damping effects of the structure and vibration attenuation resulting from non-resonant excitations. However, certain discrepancies between the finite element and experimental results are observed. These differences are attributed to the inaccuracies in the 3D printing model, the temperature sensitivity of adhesives and sensors, and defective higher frequency modes in the structure.

Fig. 6(f) shows the transmission spectrum of NSMM under a 200 g payload. Compared to the unloaded case (Fig. 3(f)–(h)), the resonance peaks of the system remain present with similar amplitude shapes, which are effectively captured by the finite element analysis. However, the amplitudes of the resonance peaks are shifted downward, causing the frequency intervals between each resonance peak to transition from vibration amplification to vibration attenuation. This shift opens multiple small damping intervals, with the damping intervals moving to lower frequencies and the bandwidth narrowing. These results are analogous to the trends observed in stiffness programming. In this work, only the transmission changes under a 200 g payload were investigated. It can be inferred that higher mass payloads would suppress vibrations more effectively and block elastic wave transmission to a greater extent.

3.4. *Influence of gradient variations on elastic wave evolution*

The combination of metamaterials with varying wave blocking capabilities significantly influences the structural performance through gradient variation. The NSMM was configured to investigate the effect of metamaterial interfacial coupling on wave transmission (Fig. 7(a)). Additionally, localized compression programming was applied to examine the impact of impedance mismatch caused by nonuniform deformation on elastic wave transmission. The bandgap onset frequencies of the S-B NSMM, C-B NSMM, and F-B NSMM are 431 Hz, 297 Hz, and 280.6 Hz, respectively (Fig. 3(b)). As shown in Fig. 7(b), the onset frequencies of all gradient combinations, except for the SB-FB-CB and CB-SB-FB configurations, are around 290 Hz, which is close to the single bandgap onset frequency of the F-B NSMM (280.6 Hz). This suggests that the F-B NSMM has a more pronounced impact on the gradient combinations. Configurations starting with the F-B NSMM exhibit lower amplitude peaks and wider troughs in their transmission spectrum, reflecting improved damping performance. The variation in the damping onset frequency highlights the enhanced low frequency wave modulation capabilities of the gradient combinations, with the first NSMM in the alignment order playing a dominant role in the interfacial coupling effect. The higher damping onset frequencies observed in the SB-CB-FB and SB-FB-CB configurations may be attributed to stronger high frequency coupling between the interfaces. By tuning the interfacial coupling effect and frequency range, different alignment orders demonstrate diverse performance characteristics. For engineering applications requiring optimized damping across multiple frequency bands, gradient metamaterials can be tailored through artificial design to achieve the desired performance.

Fig. 7(c) illustrates the transmission of these metamaterials with different width gradients within the 1000 Hz frequency range. As the width of the NS beam increases, its rigidity also increases, resulting in stronger suppression of vibration propagation. Consequently, the frequency range of the band gap shifts to higher frequencies. Fig.7(c) shows the transmission spectrum of the three metamaterials with varying width gradient configurations. For the positive width gradient, the beam with a smaller width provides a stronger NS effect and better low-frequency vibration isolation performance in the lower frequency range. As the wave is transmitted to the wider beam, the stiffness increases, which inhibits the transmission of high-frequency vibrations, leading to greater amplitude attenuation. In contrast, the negative width gradient structure starts the vibration attenuation at a lower frequency and exhibits a lower amplitude of transmission spectrum. This is because the unit cell with a width of 2 mm has a lower band gap frequency, while the unit cell with a width of 10 mm has a higher band gap frequency. Thus, the first unit cell the wave passes through has a lower band gap frequency, resulting in a lower starting frequency for wave attenuation. When the negative gradient unit is subjected to frequencies outside the bandgap and the excitation frequency, the excitation frequency induces overall vibration deformation, absorbs more vibration energy, and leads to a lower amplitude response at the receiving end. For the positive gradient structure, the low-frequency elastic wave is blocked by the 2 mm wide unit cell, and only the first unit cell deforms and absorbs a significant amount of vibration energy, with subsequent unit cells consuming less energy. Consequently, the transmission curve for the negative gradient structure moves downward. Similarly, the central negative gradient structure also starts the effective attenuation area at a lower frequency and exhibits a lower transmission value compared to the overall positive gradient structure.

The transmission amplitudes of the central negative and central positive gradient structures show that the arrangement order of the unit cells, in addition to the width gradient, affects the elastic wave attenuation amplitude.

Thickness is another critical parameter influencing the behavior of NS beams. We explored the transmission spectrum of three metamaterials with varying thickness gradients. The naming conventions follow those of the width gradients, with t representing thickness. Fig. 7(d) displays the transmission spectrum of these metamaterials within the 1000 Hz frequency range. NS beams with smaller thickness exhibit significant NS effects but have lower rigidity and a lower band gap starting frequency. In contrast, beams with larger thicknesses exhibit higher rigidity, leading to similar effects in the starting frequency and transmission curve distribution as those observed with the width gradient.

The transmission spectrum of different compression programming combinations as shown in Fig. 7(e). Positive and negative gradient structures show better vibration isolation capabilities. The damping onset frequencies for both positive and negative gradient arrangements are similar, but the difference in transmission effects between low and high frequency regions becomes pronounced with gradient arrangements. In the low frequency region of the elastic wave attenuation interval, the negative gradient arrangement demonstrates superior blocking performance compared to the positive gradient structure. When observing the vibration response of NSMMs at an excitation frequency of 180 Hz under gradient combinations, all uniformly arranged NSMMs in their initial state exhibit overall vibration. In contrast, in negative gradient programmed NSMMs, only the single cell receiving the excitation generates localized vibration. For positive gradient programmed NSMMs, only partial structural vibration displacement occurs.

The nonlinear effects induced by the programmed structure dynamically alter the bandgap properties. At the excitation frequency of 180 Hz, which lies in the passband of the programmed structure, elastic waves are not transmitted, and the structure does not vibrate.

For NSMM with negative gradient programming, at 180 Hz, the elastic wave is initially blocked by the compressed single cell, dissipating energy and confining the vibration to the local cell. Conversely, for NSMM with positive gradient programming, the elastic wave first passes through the single cell in its initial state, causing localized vibration, before being blocked by the programmed single cell, resulting in partial structural vibration displacement. Localized deformation of NSMM after programming causes an inhomogeneous impedance distribution within the metamaterial, significantly influencing the elastic wave's propagation path and energy dissipation. This effect is further amplified by the gradient arrangement, as elastic waves in different frequency bands exhibit distinct blocking characteristics within the structure. This dynamic modulation capability is crucial for bandwidth adaptive designs in engineering applications.

Metamaterial beams are extensively utilized for vibration control in applications such as vibration isolation platforms, mechanical pedestals, and precision instruments. In this work, the three proposed metamaterial structures were fabricated into beam configurations to investigate their elastic wave blocking capabilities across different frequency ranges. The Gradient Beam Structure refers to a sequential arrangement of oscillators in the order of S-B NSMM, C-B NSMM, and F-B NSMM (Fig. 7(a)). The elastic wave blocking characteristics of the beam structure feature an omnidirectional passband and forbidden band distribution, as depicted in Fig. 7(f). The NSMM beam structure exhibits two effective damping zones below an excitation frequency of 100 Hz and multiple effective damping zones extending up to 1000 Hz, where elastic waves are significantly attenuated within these zones. Among the structures, the F-B NSMM Beam Structure has the widest damping zone in the 700–1000 Hz range, demonstrating superior omnidirectional vibration isolation capabilities. In contrast, the Gradient Beam Structure leverages the advantages of all three metamaterial types, effectively combining their properties within the frequency range of 400 Hz. The distribution of damping zones in this structure is relatively uniform. At higher frequencies, the wide damping zone splits into several smaller damping zones, enabling the Gradient Beam Structure to maintain strong vibration isolation capabilities while also offering excellent load bearing capacity. The nonlinear properties of the beam material influence the transmission spectrum, further impacting the vibration isolation performance. Through topology optimization, a more efficient Gradient Beam Structure can be designed to enhance the bandgap range

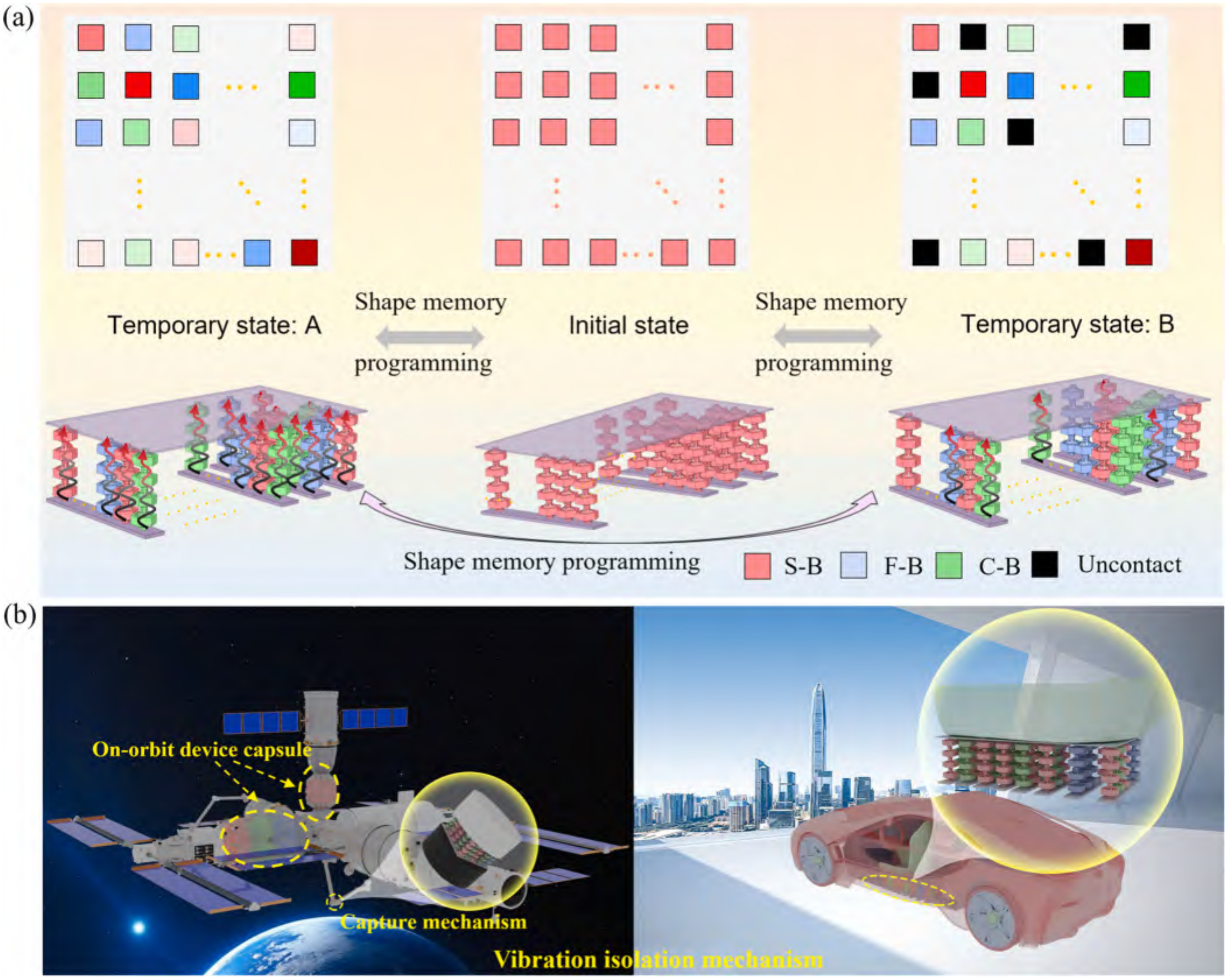

Fig. 8. NSMM strategies and applications. (a) Mechanical pixel based NSMM programming strategies for Temporary state A with modular programming control and Temporary state B with contact and separation programming, the programming state is controlled by the SMP. (b) NSMM application prospects for automotive cockpits and large space science on-orbit devices for pods and capture mechanisms.

and improve vibration isolation effects, providing promising advancements for engineering applications.

The impact response of MM is also an important aspect to investigate, particularly in evaluating their vibration suppression capabilities under nonperiodic excitation (Fig. 7(a)). This capability is quantified using the mitigation efficiency η ($a_{in-\max}$ is the maximum value of the input response, and $a_{out-\max}$ is the maximum value of the output response, $\eta = ((a_{in-\max} - a_{out-\max}) / a_{in-\max}) \cdot 100\%$, η is the mitigation efficiency.). The mitigation efficiency of NSMM under a 0.4m/s velocity impact is shown in Fig. 7(g), where all NSMM configurations demonstrate impact attenuation capabilities. Among them, the S-B NSMM exhibits weaker impact energy mitigation but is more effective in transmitting impact force. This makes it suitable for applications requiring higher stiffness and lower energy dissipation. On the other hand, the F-B NSMM demonstrates superior impact attenuation, making it better suited for applications such as impact protection, vibration damping, and energy absorption.

3.5. NSMM with mechanical pixels

The mechanical pixel for designing metamaterial structures provides a versatile method to modulate their macroscopic mechanical properties by altering the configuration and arrangement of the mechanical units. This design freedom enhances the versatility, modularity, and repairability of the structures, allowing for tailored performance across a range of applications. Programmable bandgap NSMM, utilizing mechanical pixels, offer significant advantages in modulating the frequency response of materials and designing structures with specific frequency bands or vibration control effects (Fig. 8(a)).

The mechanical pixels are designed to be modular and programmable, with the help of shape memory materials. These materials allow the configuration of NSMM's single cells to switch to a temporary shape (Shape A) to achieve desired load distribution and vibration shielding under varying operating conditions. Stiffness programming through shape memory can reduce the initial frequency of the damping operating interval significantly, from 431 Hz to 18 Hz, effectively enabling almost full band vibration isolation. Another significant strategy involves utilizing NSMM as a connecting component in systems subjected to extreme vibration loads. In these cases, NSMM switches to Temporary Shape B by enabling contact and contact separation. This decoupling concept allows NSMM to act as an independent modular vibration system, unloading strong vibration loads and protecting precision components from damage. The contact design serves both as a load distribution mechanism and as an absorber of weak vibration load energy, effectively shielding sensitive systems from excessive vibrations while maintaining operational integrity.

The proposed NSMM design holds promise for a wide range of applications, particularly in fields requiring robust vibration damping and isolation (Fig. 8(b)):

a) Automotive Industry: The mechanical pixel based NSMM can be integrated into automotive systems, such as between the chassis and the seat, to mitigate vibration disturbances. This would significantly enhance passenger comfort by isolating them from road induced vibrations, while also contributing to the safety and stability of the vehicle.
b) Space and Aerospace Sciences: The NSMM has applications in large scale installations in space, such as the vibration isolation components in on-orbit devices. The large pore size ratio of NSMM allows it to be used for creating on-orbit device cabins, where vibration isolation is critical for protecting both personnel and sensitive equipment from vibration induced damage. The modular nature of NSMM also allows for effective vibration energy absorption from contact and separation events during the operation of different compartments of on-orbit devices, ensuring the smooth operation of the system.

Furthermore, NSMM can be used to isolate vibrations transmitted by capture mechanisms in space science, protecting vibration sensitive equipment and ensuring the integrity of on-orbit devices during their capture and deployment.

4. Conclusion

In this work, based on thermally programmable shape memory polymer NS units and honeycomb oscillators made from non-thermo responsive materials, three types of NSMM with different NS units and dispersion characteristics are designed and fabricated, further exploring the performance of NSMM. Firstly, the dispersion characteristics and frequency response curves of the three metamaterials are evaluated through experiments and finite element simulations, revealing the vibration isolation capabilities and vibration contributions of the NS units. By combining shape memory materials with metamaterials, two reversible programming bandgap methods, shape programming and stiffness programming are proposed, and compared with external loading. To better achieve elastic wave control, the NSMM combinations with different gradient forms are evaluated. Finally, a lattice control strategy based on mechanical pixels is proposed. The following conclusions are drawn:

The NS unit determines the intensity and range of the NS response, and its configuration directly affects the overall equivalent stiffness of the metamaterial, thereby altering its dispersion relation and bandgap characteristics.

The S-B NSMM shows better load-bearing and energy absorption capabilities, while the F-B NSMM has stronger geometric nonlinearity and better vibration isolation ability. The evolution of the bandgap and transmission under different widths and thicknesses of the NS elements follows the same trend.

Based on the shape programmable characteristics of shape memory polymers, two methods, compression programming and torsion programming are proposed. The geometric nonlinearity induced by the programming state, along with the reduction in effective stiffness and stress variations within the structure, leads to dramatic evolution of the bandgap, helping to open low frequency bandgaps and widen the bandwidth. Based on the stiffness programming characteristics of shape memory polymers, an NSMM stiffness programming method is proposed, where increasing temperature causes a nonlinear decrease in the bandgap, achieving effective vibration isolation from 0-1000 Hz. Boundary conditions with effective loads are also verified to effectively suppress vibration transmission.

The elastic wave suppression capabilities of NSMM combinations with different gradients are also studied. The starting frequency of the effective vibration reduction range for different gradient combinations is determined by the unit cell with the lowest starting frequency of the bandgap for that combination, and it is close to the lower frequency limit of the bandgap. Different combination sequences only affect the value of the transmission curve. Elastic waves at specific excitation frequencies are blocked within the unit cell of a specific bandgap and cannot cause displacement responses in subsequent unit cells.

A lattice control strategy based on mechanical pixels is proposed. The mutual transformation between NS elements and the two programming schemes offer customized solutions for different force and vibration needs, providing valuable references for the development of metamaterials that can meet specific functional requirements. Therefore, this study provides a reliable guide for applying programmable NSMM to space-based on-orbit devices and the automotive industry.

CRediT authorship contribution statement

Wenyou Zha: Writing – original draft, Investigation, Formal analysis. **Rui Yang:** Methodology, Investigation. **Yongtao Yao:** Writing – review & editing, Supervision, Project administration, Methodology, Funding acquisition. **Yanju Liu:** Writing – review & editing,

Supervision, Project administration. **Jinsong Leng:** Writing – review & editing, Supervision, Project administration, Funding acquisition.

Declaration of competing interest

The authors declare that they have no known competing financial interests or personal relationships that could have appeared to influence the work reported in this paper.

Acknowledgments

This work was financially supported by the National Key R&D Program of China (Grant No. 2022YFB3805700), and the National Natural Science Foundation of China (Grant No. 12272112).

Appendix A. Demonstration of shape memory in NS beams and the experimental setup of NSMM

We use a simple demonstration (Fig. A1) to illustrate the shape memory mechanism. By subjecting the three types of NS beams to thermal programming, temporary shapes are obtained and converted into another beam form, with all three types of beams being interchangeable. Finally, under a second thermal stimulus, the beams recover to their permanent shapes, completing one memory cycle.

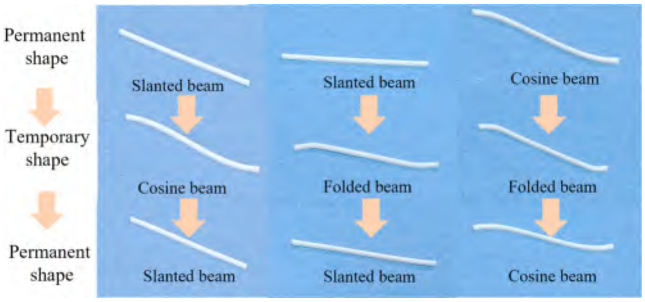

Fig. A1. Shape memory programming for NS elements. The NS element is shaped in the rubbery state, retains the temporary shape in the glassy state, and recovers the permanent shape upon reheating.

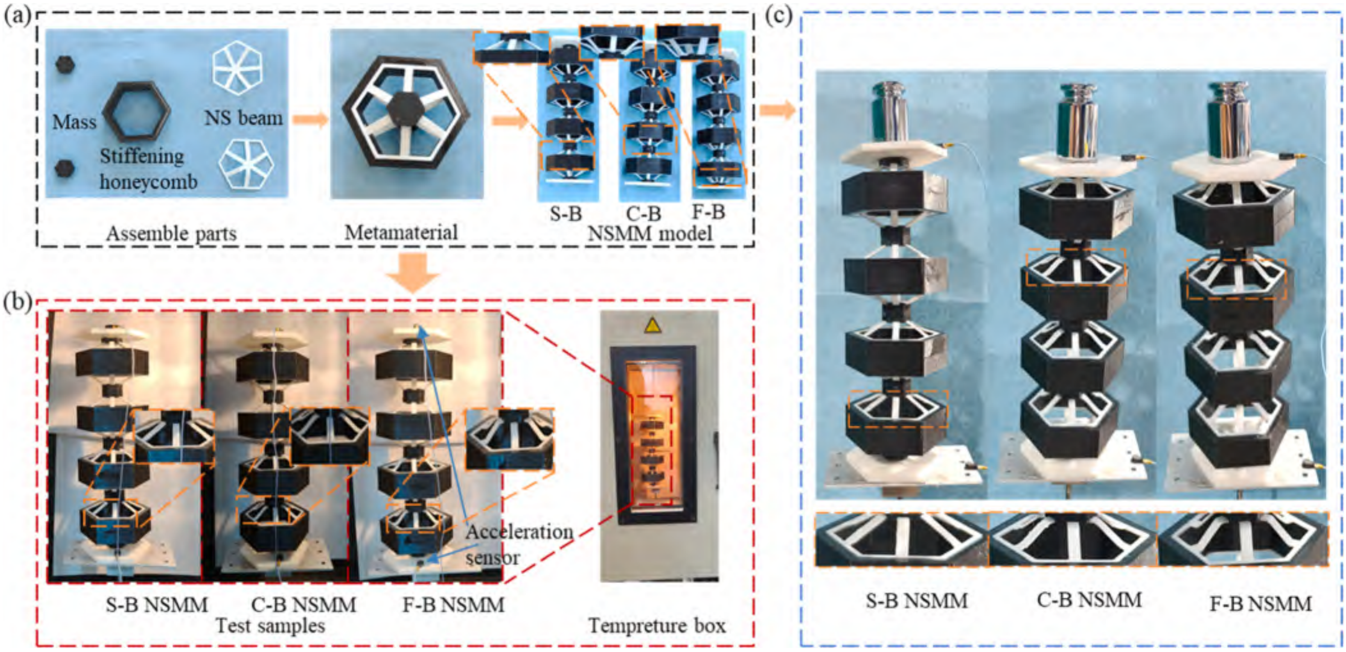

Fig. A2. NSMM assembly process and experimental setup. (a) NSMM assembly process. NSMM consists of NS elements, honeycomb structure, and a mass block. (b) NSMM shape memory stiffness programmed vibration testing. The test places the NSMM inside a temperature-controlled chamber to regulate the stiffness of the SMP by adjusting the temperature. Vibration signals are input at the bottom of the NSMM and output at the top. (c) NSMM payload vibration testing. The applied payload is realized by attaching a 200g weight on top of the NSMM.

The components of the NSMM were fabricated and assembled using 3D printing to obtain our test specimen (Fig. A2(a)). The NS elements were made of white PLA-SMP material, while the rigid honeycomb and resonator were made of black ABS material. The specimen was connected to a vibration excitation system and placed inside a temperature-controlled chamber to investigate the vibration response of the NSMM at different temperatures. One end of the specimen was connected to the excitation system, while a 200g weight was fixed to the other end to study the vibration response of the NSMM under mass suppression. Fig. A2(b) and (c) show more experimental details.

Fig. A3 presents a simple demonstration of the shape memory process of the NSMM. The NSMM is programmed under a thermal environment to obtain a temporary shape and returns to its permanent shape upon subsequent thermal activation.

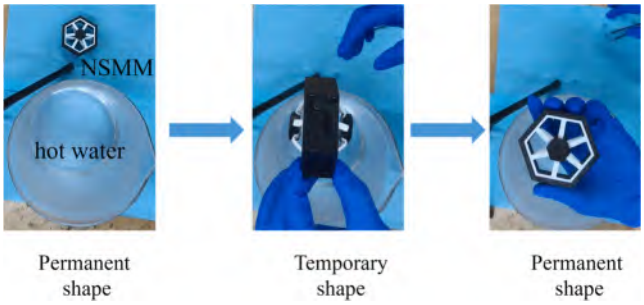

Fig. A3. Shape memory programming for NSMM. F-B NSMM is programmed by the shape in the thermal state, and the permanent shape can be restored by heating again.

Appendix B. Bandgap and vibrational modes of NSMM

Fig. B1 shows the dispersion curves and vibration modes of the C-B NSMM and F-B NSMM. The F-B NSMM has a lower starting bandgap and a wider bandwidth within the 0-3000Hz range. The vibration modes of the two NSMMs are similar, with the first mode (B1 and C1) and the sixth mode (B6 and C6) exhibiting overall deformation. Other modes only show displacement generated by the negative stiffness elements, while the second mode (B2 and C2) is a torsional effect.

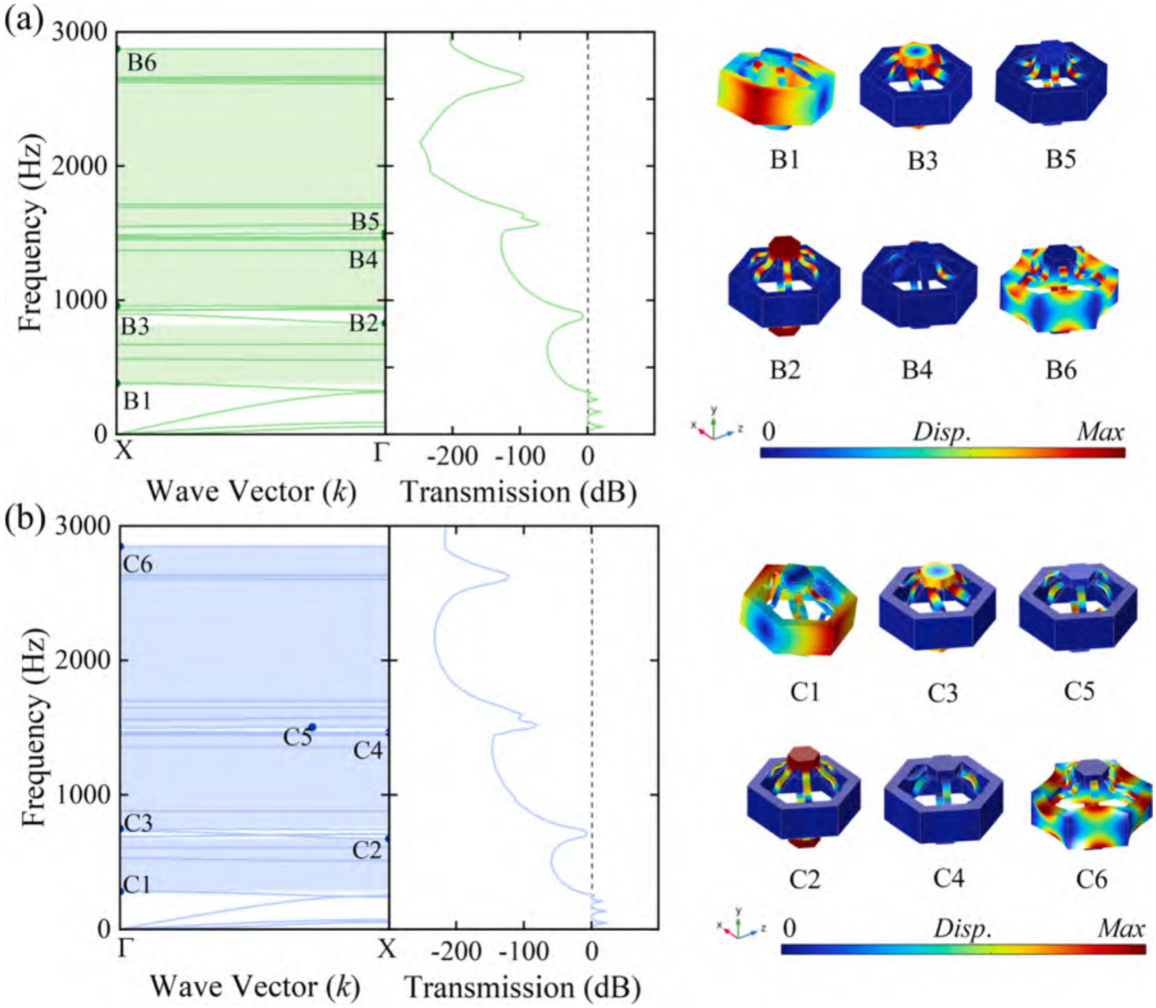

Fig. B1. Metamaterial band gap and vibrational modes. (a) Energy band transfer curves and vibrational modes for C-B NSMM. (b) Energy band transfer curves and vibrational modes for F-B NSMM. The modes corresponding to the starting frequencies (B1, C1) and cutoff frequencies (B6, C6) are global modes, while the deformation of the other modes is concentrated in the negative stiffness elements. The F-B NSMM exhibits a lower starting frequency and a wider bandgap.

Appendix C. Bandgap evolution and transmission spectrum in shape memory programming of NSMM

The deformation process is divided into three stages: Stage 1 (positive stiffness, elastic deformation), Stage 2 (NS, elastic destabilization deformation), and Stage 3 (positive stiffness, plastic deformation in the dense stage). The compression mechanics curves of the S-B NSMM show that the peak values gradually increase with the width and thickness of the ligaments, enhancing the NS characteristics and energy absorption capacity. Specifically, the width change does not affect the zero potential energy point. The initial stiffness of the C-B NSMM is lower than that of the S-B NSMM, but the NS stage starts earlier, suggesting that the geometric design of the cosine beams is more prone to destabilization. The initial stiffness of the F-B NSMM is the lowest, indicating that the folded beams are more susceptible to bending deformation.

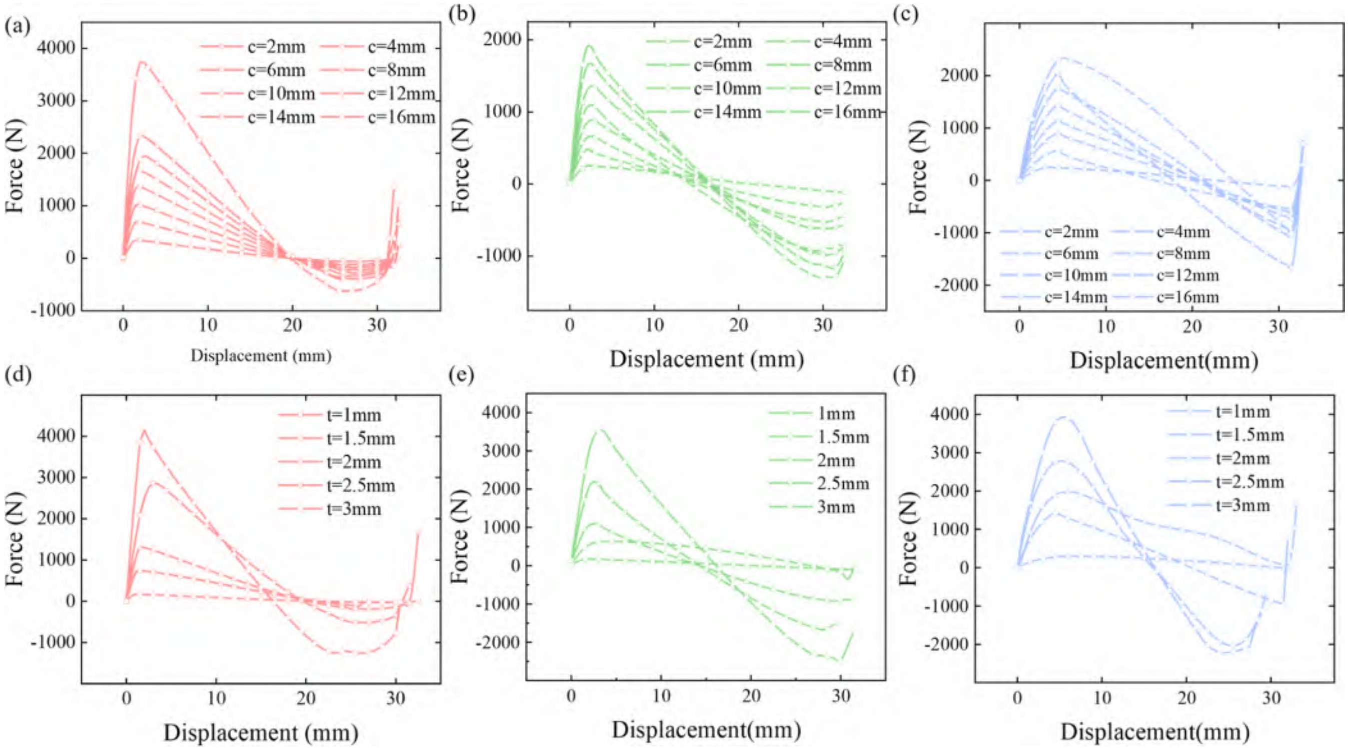

Fig. C1. NSMM quasi-static compression. Mechanical properties of (a) S-B NSMM, (b) C-B NSMM and (c) F-B NSMM at different widths. Mechanical properties of (d) S-B NSMM, (e) C-B NSMM and (f) F-B NSMM at different thicknesses.

To investigate the evolution of band gaps in NSMMs under shape programming, displacement was applied to both ends of the NSMM at 70 °C, and the bandgap evolution under different compressed configurations was studied at 25 °C. Taking the S-B NSMM as an example, Fig. C2 shows its band gap distribution and vibration displacement under different compression programming states. It can be seen that deformation significantly affects the frequency range and bandwidth of the band gaps. This is due to geometric nonlinear changes induced by compression, resulting in reduced effective stiffness and changes in internal stress within the structure. Multiple branches form at low frequencies, effectively opening low-frequency bandgaps, and with increasing deformation, the band gap evolution becomes pronounced. At the same time, the high-frequency branches gradually flatten, indicating that the group velocity is nearly zero. Observing the vibrational diagrams under different programming states, the excitation frequency of 250Hz is within the pass band of the initial state, allowing elastic waves to pass through the S-B NSMM completely and resulting in an overall vibration displacement, manifesting as vibration amplification. However, for the compressed programming state, 250Hz falls within the bandgap, so the elastic wave is attenuated within the first unit cell and cannot induce an overall displacement.

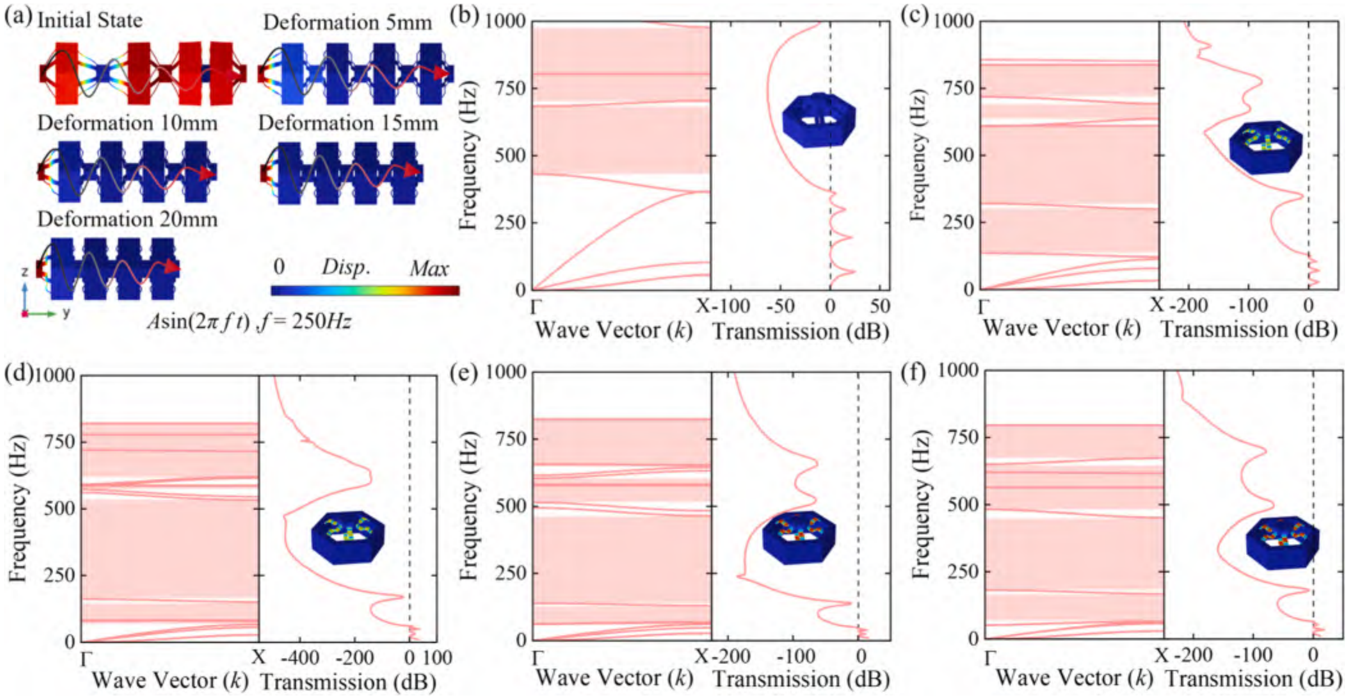

Fig. C2. S-B NSMM compression programming bandgap. (a) Vibrational diagrams. The excitation frequency is outside the bandgap, it induces global deformation displacement of the S-B NSMM. The excitation frequency is within the bandgap, it only causes unit cell deformation. Bandgap and transmission spectrum of (b) Initial state, (c) 5 mm, (d) 10 mm, (e) 15 mm, and (g) 20 mm. Geometric nonlinearity and internal structural stress under compression programming cause significant bandgap evolution, including bandgap downshift, bandwidth widening, emergence of new bandgaps, and high frequency branch flattening.

The evolution of band gaps in the torsional state of the NSMM was also investigated using the same method. Fig. C3 shows the bandgap distribution and vibration displacement under different torsional programming states. It can be seen that torsional deformation also has a significant effect on the frequency range and bandwidth of the band gaps. Multiple branches form at low frequencies, effectively opening low-frequency band gaps, and with increasing deformation, the band gap evolution becomes pronounced. Observing the vibrational diagrams under different programming states, the excitation frequency of 180Hz is located in the pass band of the initial structure and in the bandgap of the programmed state, causing similar vibration displacements. However, the vibration displacement caused by torsion only exists in the NS elements and the resonators.

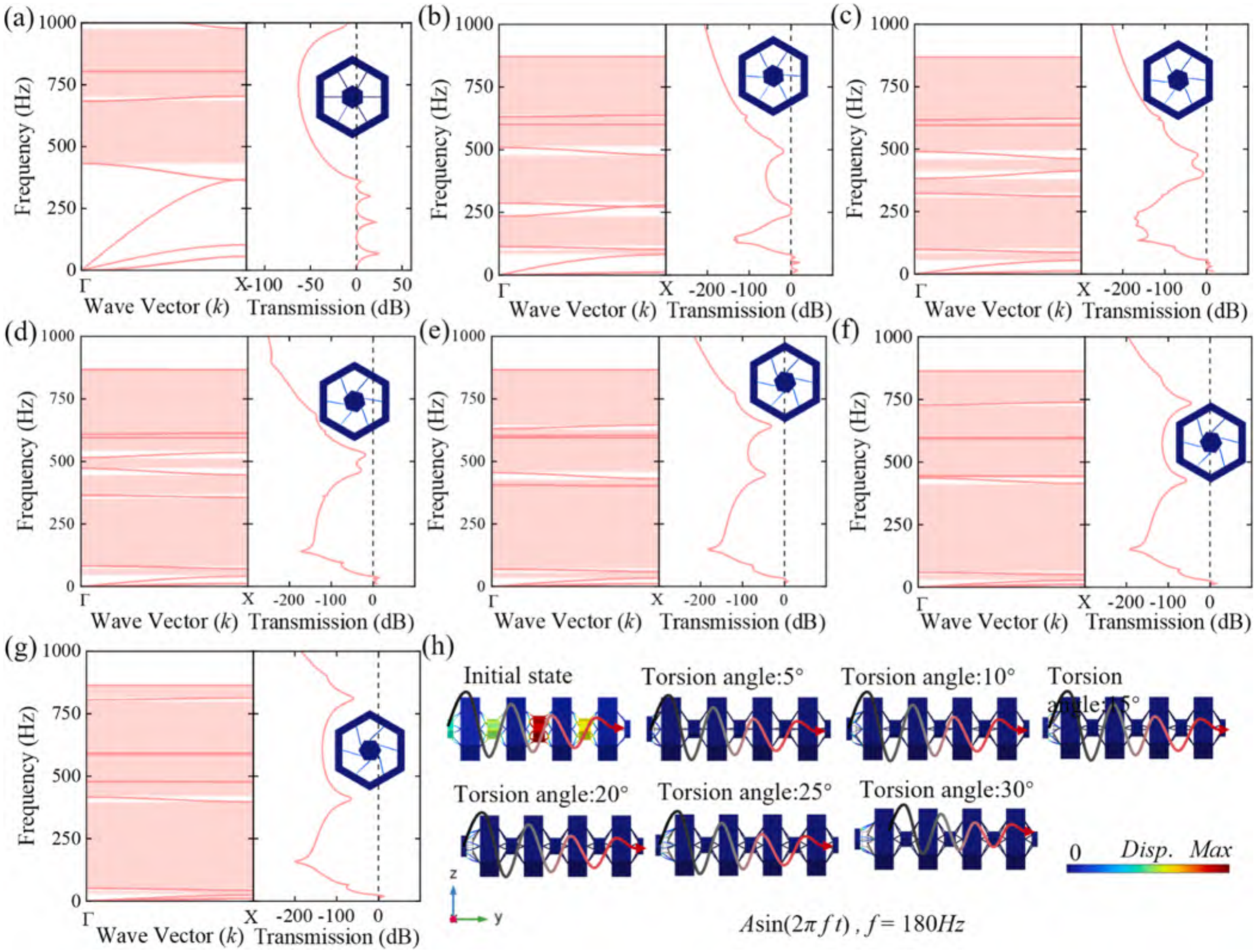

Fig. C3. S-B NSMM torsion programming bandgap and transmission evolution. Bandgap and transmission spectrum of (a) Initial state, (b) Torsion angle of 5°, (c) Torsion angle of 10°, (d) Torsion angle of 15°, (e) Torsion angle of 20°, (f) Torsion angle of 25°, and (g) Torsion angle of 30°. (h) Vibrational diagrams. Geometric nonlinearity, internal structural stress, and symmetry breaking under torsion programming lead to significant bandgap evolution, including bandgap downshift, bandwidth expansion, emergence of new bandgaps, and high frequency branch flattening.

Fig. C4 presents the transmission spectrum colormap of the NSMM under different temperature conditions. The evolution of the transmission spectrum shows a white band-like variation trend, which corresponds to the bandgap changes under this condition.

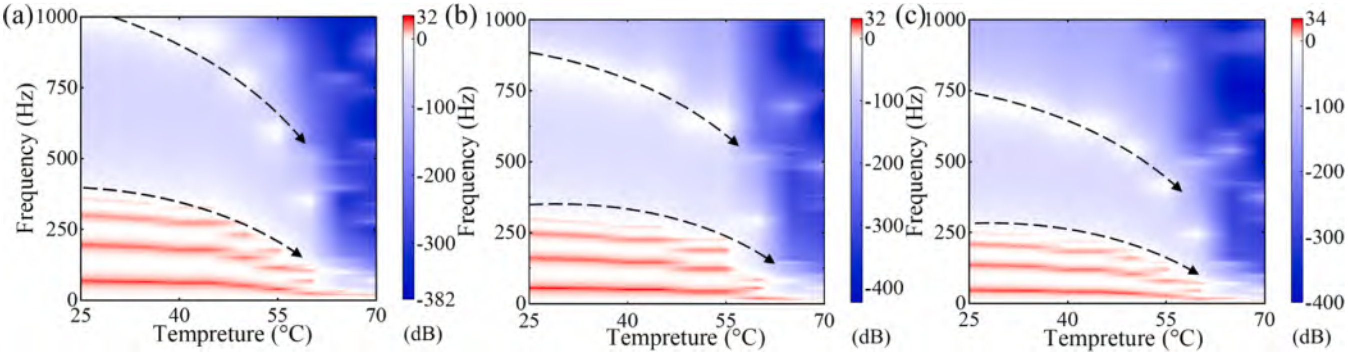

Fig. C4. Evolution of NSMM stiffness programming transmission spectrum. (a) S-B NSMM, (b) C-B NSMM, and (c) F-B NSMM transmission spectrum under stiffness programming, 25 °C to 75°C. Under stiffness programming, the stiffness of PLA-SMP decreases with increasing temperature, leading to a reduction in bandgap nonlinearity. Correspondingly, the attenuation region in the transmission spectrum shows a nonlinear decrease.

Appendix D. Bandgap evolution in shape memory programming of NSMM

The flexibility of NSMM is changed in the programmed state, and the nonlinear control equation of the NS beam is a typical margin problem. It can be solved in segments based on Euler Bernoulli beam theory. The NS elements of the three metamaterials in this study determine the stiffness of the structure, and the spring stiffness of the NSMM is solved, taking the slanted beam as an example. The basic elements of deformation and the deformation mode are shown in Fig. D1.

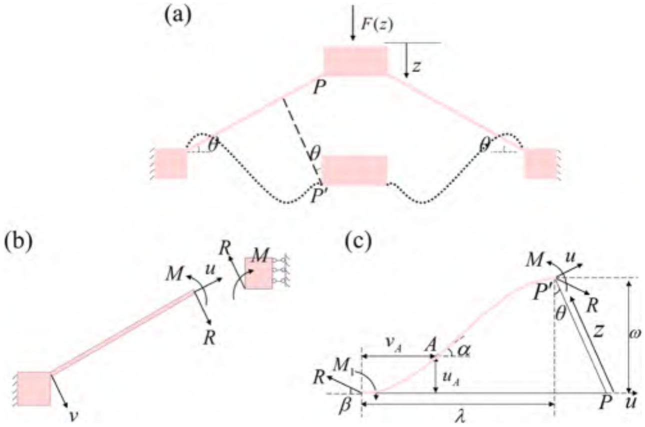

Fig. D1. Slanted beam model. (a) Basic deformation unit. (b) Force analysis. (c) Equivalent model. Calculate the equivalent stiffness of the deformed S-B NSMM.

The equilibrium equation for equivalent model can be expressed as:

$$EI\frac{d\alpha}{ds} = M_1 + Rv_A\cos\beta - Ru_A\sin\beta, \tag{D.1}$$

where u_A and v_A are the horizontal and vertical coordinates of point A, EI is the bending stiffness, β is the horizontal angle of the force, α is the horizontal angle of A, and s is the line coordinate.

According to the geometric relationship, we have $\cos\alpha = du_A/ds$,$\sin\alpha = dv_A/ds$, substituting into Eq(D.1) and taking the derivative for the line coordinatess,

$$EI\frac{d^2\alpha}{ds^2} = R\sin\alpha\cos\beta - R\cos\alpha\sin\beta. \tag{D.2}$$

Integrate Eq(D.2) to the angle α, we have,

$$\frac{EI}{2}\left(\frac{d\alpha}{ds}\right)^2 = -R\cos\alpha\cos\beta - R\sin\alpha\sin\beta + C, \tag{D.3}$$

C is a constant, which can be collapsed to give,

$$ds = \frac{\sqrt{EI}}{\sqrt{-2R_e\cos(\alpha-\beta)+2C}}d\alpha. \tag{D.4}$$

Conducting Eq(D.4) to integrate over the beam, $L = \int_0^L ds$.

The coordinates of the point $P'$are,

$$\omega_b = \int_0^L \sin\alpha ds = \int_0^{\alpha_m}\frac{\sqrt{EI}\sin\alpha}{\sqrt{-2R\cos(\alpha-\beta)+2C}}d\alpha + \int_{\alpha_m}^0\frac{\sqrt{EI}\sin\alpha}{\sqrt{-2R\cos(\alpha-\beta)+2C}}d\alpha, \tag{D.5}$$

$$\lambda_b = \int_0^L \cos\alpha ds = \int_0^{\alpha_m}\frac{\sqrt{EI}\cos\alpha}{\sqrt{-2R\cos(\alpha-\beta)+2C}}d\alpha + \int_{\alpha_m}^0\frac{\sqrt{EI}\cos\alpha}{\sqrt{-2R\cos(\alpha-\beta)+2C}}d\alpha, \tag{D.6}$$

α_m is the maximum horizontal angle on the beam. Define the constant k and the variable φ,

$$\begin{cases} C = R(2k^2-1) \\ \cos\left(\dfrac{\beta-\alpha}{2}\right) = k\sin\varphi. \end{cases} \tag{D.7}$$

Substituting k and φ into L, we have:

$$\sqrt{\mu_L} = \sqrt{\frac{L^2R}{EI}} = \int_{\varphi_1}^{\varphi_2}\frac{d\varphi}{\sqrt{1-k^2\sin^2\varphi}}, \tag{D.8}$$

φ_1 and φ_2 are determined by the flexural modes of the beam, n is the flexural mode, and only the first two orders of modes are considered in this study. When n is 1, $\varphi_2 = n\pi - \varphi_1$; when n is 2, $\varphi_2 = n\pi + \varphi_1$.

To simplify the computation introduce the incomplete elliptic integrals $G(k, \varphi)$and $H(k, \varphi)$, defined as follows:

$$\begin{cases} G(k,\varphi) = \int_0^{\varphi} \frac{d\delta}{\sqrt{1-k^2\sin^2\delta}} \\ H(k,\varphi) = \int_0^{\varphi} \sqrt{1-k^2\sin^2\delta}\,d\delta. \end{cases} \tag{D.9}$$

Then Eq(D.5) and Eq(D.6) are rewritten as:

$$\frac{\omega_b}{L} = -\frac{1}{\sqrt{\mu_L}}\{\sin\beta[2H(k,\varphi_2) - 2H(k,\varphi_1) - G(k,\varphi_2) + G(k,\varphi_1)] + 2k\cos\beta(\cos\varphi_1 - \cos\varphi_2)\}, \tag{D.10}$$

$$\frac{\lambda_b}{L} = -\frac{1}{\sqrt{\mu_L}}\{\cos\beta[2H(k,\varphi_2) - 2H(k,\varphi_1) - G(k,\varphi_2) + G(k,\varphi_1)] + 2k\sin\beta(\cos\varphi_2 - \cos\varphi_1)\}, \tag{D.11}$$

which $\sqrt{\mu_L} = G(k,\varphi_2) - G(k,\varphi_1)$.

Considering the Poisson effect, the axial strain of the inclined beam,

$$\varepsilon_L = \frac{R\cos(\beta-\alpha)}{EA}, \tag{D.12}$$

EA is the axial compressive stiffness of the inclined beam, the projection of Eq(D.12), and the integration of the line coordinates s to obtain the displacement at the point P' of the flexural beam after axial loading,

$$\frac{\omega_a}{L} = \frac{1}{L}\int_0^L \varepsilon\sin\alpha ds = \frac{\sqrt{\mu_L}}{\lambda_L^2}\int_{\varphi_1}^{\varphi_2} \frac{r^2\cos(\alpha-\beta)\sin\alpha}{\sqrt{1-k^2\sin^2\varphi}}d\varphi, \tag{D.13}$$

$$\frac{\lambda_a}{L} = \frac{1}{L}\int_0^L \varepsilon\cos\alpha ds = \frac{\sqrt{\mu_L}}{\lambda_L^2}\int_{\varphi_1}^{\varphi_2} \frac{r^2\cos(\alpha-\beta)\cos\alpha}{\sqrt{1-k^2\sin^2\varphi}}d\varphi. \tag{D.14}$$

In the above equation, λ_L is the aspect ratio, defined as $\lambda_L^2 = AL^2/I$.

Superimpose the bending moment and axial force effects to obtain the total vertical and horizontal displacements of P',

$$\omega = \omega_b + \omega_a, \tag{D.15}$$

$$\lambda = \lambda_b + \lambda_a. \tag{D.16}$$

For the given displacement deformations ω and λ, the corresponding k and φ can be deduced from the force relationship as follows:

$$F_z = 2R\sin(\beta-\alpha). \tag{D.17}$$

According to the geometric relation we have:

$$z = \sqrt{(L-\lambda)^2 + \omega^2}. \tag{D.18}$$

Eq(D.8), Eq(D.15), Eq(D.16) are established by solving for k and β given the deterministic displacements.

Therefore, the stiffness of the structure $k_T(z)$ can be expressed as:

$$k_T(z) = dF(z)/dz. \tag{D.19}$$

For stiffness programming, the corresponding structural stiffness can be solved by solving the modulus of elasticity under the influence of temperature. For compression shape programming, the structural stiffness can be solved with the help of Eq(D.19).

Data availability

Data will be made available on request.

References

[1] Kadic M, Milton GW, van Hecke M, Wegener M. 3D metamaterials. Nat Rev Phys 2019;1:198–210. https://doi.org/10.1038/s42254-018-0018-y.

[2] Jiao P, Mueller J, Raney JR, Zheng X, Alavi AH. Mechanical metamaterials and beyond. Nat Commun 2023;14:6004. https://doi.org/10.1038/s41467-023-41679-8.

[3] Shi Y, Song Q, Toftul I, Zhu T, Yu Y, Zhu W, Tsai DP, Kivshar Y, Liu AQ. Optical manipulation with metamaterial structures. Appl Phys Rev 2022;9:031303. https://doi.org/10.1063/5.0091280.

[4] Akbari-Farahani F, Ebrahimi-Nejad S. From defect mode to topological metamaterials: A state-of-the-art review of phononic crystals & acoustic metamaterials for energy harvesting. Sens Actuators A: Phys 2024;365:114871. https://doi.org/10.1016/j.sna.2023.114871.

[5] Fan C, Wu C-L, Wang Y, Wang B, Wang J. Thermal metamaterials: from static to dynamic heat manipulation. Phys Rep 2024;1077:1–111. https://doi.org/10.1016/j.physrep.2024.05.004.

[6] Karami B, Ghayesh MH. Dynamics of graphene origami-enabled auxetic metamaterial beams via various shear deformation theories. Int J Eng Sci 2024;203:104123. https://doi.org/10.1016/j.ijengsci.2024.104123.

[7] Wang J, Dai G, Huang J. Thermal metamaterial: fundamental, application, and outlook. iScience 2020;23. https://doi.org/10.1016/j.isci.2020.101637.

[8] Soukoulis CM, Linden S, Wegener M. Negative refractive index at optical wavelengths. Science 2007;315:47–9. https://doi.org/10.1126/science.1136481.

[9] Ma J, Shi Y, Meng Q, Yao B, Wang J, Duan J, Zhang B, Liu Y. A radar-infrared compatible stealth metamaterial with bird's nest morphology. J Alloys Compd 2024;986:174137. https://doi.org/10.1016/j.jallcom.2024.174137.

[10] Deng J, Zheng L. Noise reduction via three types of acoustic black holes. Mech Syst Signal Process 2022;165:108323. https://doi.org/10.1016/j.ymssp.2021.108323.

[11] Han H, Sorokin V, Tang L, Cao D. Origami-based tunable mechanical memory metamaterial for vibration attenuation. Mech Syst Signal Process 2023;188:110033. https://doi.org/10.1016/j.ymssp.2022.110033.

[12] Wu L, Li B, Zhou J. Isotropic negative thermal expansion metamaterials. ACS Appl Mater Interfaces 2016;8:17721–7. https://doi.org/10.1021/acsami.6b05717.

[13] Pan Y, Zhou Y, Wang M, Gao Q, Sun B. A novel reinforced cylindrical negative stiffness metamaterial for shock isolation: analysis and application. Int J Solids Struct 2023;279:112391. https://doi.org/10.1016/j.ijsolstr.2023.112391.

[14] Ou J, Ma Z, Peters J, Dai S, Vlavianos N, Ishii H. KinetiX - designing auxetic-inspired deformable material structures. Comput Graph 2018;75:72–81. https://doi.org/10.1016/j.cag.2018.06.003.

[15] Zhang L, Yan S, Liu W, Liu Y, Cai W, Zhang Z, Zhou J. Mechanical metamaterials with negative Poisson's ratio: A review. Eng Struct 2025;329:119838. https://doi.org/10.1016/j.engstruct.2025.119838.

[16] Wang S, Zeng Y, Wang C, Sun S, Mei C, Pan M. Negative Poisson's ratio structural cellulose aerogel with excellent impact resistance. Chem Eng J 2025;507:160492. https://doi.org/10.1016/j.cej.2025.160492.

[17] Correa DM, Klatt T, Cortes S, Haberman M, Kovar D, Seepersad C. Negative stiffness honeycombs for recoverable shock isolation. Rapid Prototyp J 2015;21:193–200. https://doi.org/10.1108/RPJ-12-2014-0182.

[18] Rocklin DZ, Zhou S, Sun K, Mao X. Transformable topological mechanical metamaterials. Nat Commun 2017;8:14201. https://doi.org/10.1038/ncomms14201.

[19] Padilla WJ, Averitt RD. Imaging with metamaterials. Nat Rev Phys 2022;4:85–100. https://doi.org/10.1038/s42254-021-00394-3.

[20] Cummer SA, Christensen J, Alù A. Controlling sound with acoustic metamaterials. Nat Rev Mater 2016;1:16001. https://doi.org/10.1038/natrevmats.2016.1.

[21] Tan T, Yan Z, Zou H, Ma K, Liu F, Zhao L, Peng Z, Zhang W. Renewable energy harvesting and absorbing via multi-scale metamaterial systems for internet of things. Appl Energy 2019;254:113717. https://doi.org/10.1016/j.apenergy.2019.113717.

[22] Dudek KK, Iglesias Martínez JA, Ulliac G, Hirsinger L, Wang L, Laude V, Kadic M. Micro-scale mechanical metamaterial with a controllable transition in the Poisson's ratio and band gap formation. Adv Mater 2023;35:2210993. https://doi.org/10.1002/adma.202210993.

[23] Dalela S, S BP, Jena DP. A review on application of mechanical metamaterials for vibration control. Mech Adv Mater Struct 2022;29:3237–62. https://doi.org/10.1080/15376494.2021.1892244.

[24] Alomarah A, Yuan Y, Ruan D. A bio-inspired auxetic metamaterial with two plateau regimes: compressive properties and energy absorption. Thin-Walled Struct 2023;192:111175. https://doi.org/10.1016/j.tws.2023.111175.

[25] Surjadi JU, Gao L, Du H, Li X, Xiong X, Fang NX, Lu Y. Mech Metamater Their Eng Appl Adv Eng Mater 2019;21:1800864. https://doi.org/10.1002/adem.201800864.

[26] Dong P, Hu J, Gong Z, Li Y, Liu J, Cao J, Lin C, Ding W. Design strategies of cementitious metamaterials (CMs) with tunable bandgaps: density customization and geometric optimization. J Build Eng 2024;95:110132. https://doi.org/10.1016/j.jobe.2024.110132.

[27] Krushynska AO, Miniaci M, Bosia F, Pugno NM. Coupling local resonance with Bragg band gaps in single-phase mechanical metamaterials. Extreme Mech Lett 2017;12:30–6. https://doi.org/10.1016/j.eml.2016.10.004.

[28] Li H, Hu Y, Huang H, Chen J, Zhao M, Li B. Broadband low-frequency vibration attenuation in 3D printed composite meta-lattice sandwich structures. Compos B: Eng 2021;215:108772. https://doi.org/10.1016/j.compositesb.2021.108772.

[29] Zhao S, Zhang Y, Zhang Y, Yang J, Kitipornchai S. Vibrational characteristics of functionally graded graphene origami-enabled auxetic metamaterial beams based on machine learning assisted models. Aerosp Sci Technol 2022;130:107906. https://doi.org/10.1016/j.ast.2022.107906.

[30] Elmadih W, Chronopoulos D, Syam WP, Maskery I, Meng H, Leach RK. Three-dimensional resonating metamaterials for low-frequency vibration attenuation. Sci Rep 2019;9:11503. https://doi.org/10.1038/s41598-019-47644-0.

[31] Chen D, Zi H, Li Y, Li X. Low frequency ship vibration isolation using the band gap concept of sandwich plate-type elastic metastructures. Ocean Eng 2021;235:109460. https://doi.org/10.1016/j.oceaneng.2021.109460.

[32] Muhammad CWLim. Ultrawide bandgap by 3D monolithic mechanical metastructure for vibration and noise control. Arch Civ Mech Eng 2021;21:52. https://doi.org/10.1007/s43452-021-00201-x.

[33] Oudich M, Gerard NJRK, Deng Y, Jing Y. Tailoring structure-borne sound through bandgap engineering in phononic crystals and metamaterials: A comprehensive review. Adv Funct Mater 2023;33:2206309. https://doi.org/10.1002/adfm.202206309.

[34] Sugino C, Ruzzene M, Erturk A. Merging mechanical and electromechanical bandgaps in locally resonant metamaterials and metastructures. J Mech Phys Solids 2018;116:323–33. https://doi.org/10.1016/j.jmps.2018.04.005.

[35] Gao Y, Wang L, Sun W, Wu K, Hu H. Ultrawide bandgap in metamaterials via coupling of locally resonant and Bragg bandgaps. Acta Mech 2022;233:477–93. https://doi.org/10.1007/s00707-021-03122-1.

[36] Zhou Y, Ye L, Chen Y. Developing three-dimensional mechanical metamaterials with tailorable bandgaps for impact mitigation. J Phys D Appl Phys 2024;57:195501. https://doi.org/10.1088/1361-6463/ad2478.

[37] Nash LM, Kleckner D, Read A, Vitelli V, Turner AM, Irvine WTM. Topological mechanics of gyroscopic metamaterials. Proc Natl Acad Sci 2015;112:14495–500. https://doi.org/10.1073/pnas.1507413112.

[38] Wang Q, Miao L, Zheng H, Xiao P, Zhang B, Lei K. Bandgap characteristic and bandgap expansion of a petal-shaped metamaterial. Solid State Commun 2024;389:115563. https://doi.org/10.1016/j.ssc.2024.115563.

[39] Ruan H, Li D. Band gap characteristics of bionic acoustic metamaterials based on spider web. Eng Struct 2024;308:118003. https://doi.org/10.1016/j.engstruct.2024.118003.

[40] Cao Z-Y, Sai H, Wang W, Yang K-C, Wang L, Lv P, Duan H, Huang T-Y. Bioinspired microhinged actuators for active mechanism-based metamaterials. Adv Sci 2025;12:2407231. https://doi.org/10.1002/advs.202407231.

[41] Li Z, Wang X, Zeng K, Guo Z, Li C, Yu X, Ramakrishna S, Wang Z, Lu Y. Unprecedented mechanical wave energy absorption observed in multifunctional bioinspired architected metamaterials. NPG Asia Mater 2024;16:45. https://doi.org/10.1038/s41427-024-00565-5.

[42] Enayat Jazi A, Mahdiabadi MKaramooz. Numerical and experimental investigation of bio-inspired lattice structures based on Camphor tree blossoms for vibration mitigation. Structures 2025;76:109001. https://doi.org/10.1016/j.istruc.2025.109001.

[43] Yan B, Ling P, Miao L, Yu N, Sun J, Li Q. Ultra-low frequency vibration isolation of cockroach-inspired structures with electromagnetic shunt damping enhanced by geometric nonlinearity. IEEE/ASME Trans Mechatron 2024;29:476–86. https://doi.org/10.1109/TMECH.2023.3287915.

[44] Xu J, Xiang S, Boyang Z, Hanjie Y, Dan S, Jie Z, Xiao H. 3D-printed multifunctional chiral metamaterial with invariant sound absorption under large deformation and low-frequency vibration control. Virtual Phys Prototyp 2024;19:e2425386. https://doi.org/10.1080/17452759.2024.2425386.

[45] Sun P, Guo H, Jin F, Zhang Z, Liu N, Yuan T, Ma L, Wang Y. Mechanics and extreme low-frequency band gaps of auxetic hexachiral acoustic metamaterial with internal resonant unit. Appl Acoust 2022;200:109046. https://doi.org/10.1016/j.apacoust.2022.109046.

[46] Xu Z-L, Wang Y-Q, Zhu R, Chuang K-C. Torsional bandgap switching in metamaterials with compression–torsion interacted origami resonators. J Appl Phys 2021;130:045105. https://doi.org/10.1063/5.0056179.

[47] An X, Lai C, He W, Fan H. Three-dimensional meta-truss lattice composite structures with vibration isolation performance. Extreme Mech Lett 2019;33:100577. https://doi.org/10.1016/j.eml.2019.100577.

[48] An X, Yuan X, Sun G, Hou X, Fan H. Design of lattice cylindrical shell meta-structures for broadband vibration reduction and high load-bearing capacity. Thin-Walled Struct 2024;197:111647. https://doi.org/10.1016/j.tws.2024.111647.

[49] Zhou S, Xu P, Hou B, Ren Z. Dynamic characteristics analysis of bilayer bio-inspired X-shaped vibration isolation structure. Int J Non Linear Mech 2023;154:104447. https://doi.org/10.1016/j.ijnonlinmec.2023.104447.

[50] Li M, Jing X. A bistable X-structured electromagnetic wave energy converter with a novel mechanical-motion-rectifier: design, analysis, and experimental tests. Energy Convers Manag 2021;244:114466. https://doi.org/10.1016/j.enconman.2021.114466.

[51] Wei W, Guan F, Fang X. A low-frequency and broadband wave-insulating vibration isolator based on plate-shaped metastructures. Appl Math Mech 2024;45:1171–88. https://doi.org/10.1007/s10483-024-3160-6.

[52] Wang Q, Miao L, Zheng H, Xiao P, Zhang B. Design of elastic metamaterial plate and application in subway vibration isolation. Appl Phys A 2024;130:557. https://doi.org/10.1007/s00339-024-07691-5.

[53] Xin Y-j, Huang R-n, Li P, Qian Q, Yan Q, Sun Y-t, Ding Q, Huang Y-j, Cheng S-l. Labyrinthine acoustic metamaterials with triangular self-similarity for low-frequency sound insulation at deep subwavelength dimensions. Results Phys 2023;54:107151. https://doi.org/10.1016/j.rinp.2023.107151.

[54] Cui H, Liu C, Hu H. Research on low-frequency noise control based on fractal coiled acoustic metamaterials. Shock Vib 2022;2022:2083563. https://doi.org/10.1155/2022/2083563.

[55] Miyazawa Y, Chen C-W, Chaunsali R, Gormley TS, Yin G, Theocharis G, Yang J. Topological state transfer in Kresling origami. Commun Mater 2022;3:62. https://doi.org/10.1038/s43246-022-00280-0.

[56] Hu Z, Wei Z, Wang K, Chen Y, Zhu R, Huang G, Hu G. Engineering zero modes in transformable mechanical metamaterials. Nat Commun 2023;14:1266. https://doi.org/10.1038/s41467-023-36975-2.

[57] Z. Meng, M. Liu, H. Yan, G.M. Genin, C.Q. Chen, Deployable mechanical metamaterials with multistep programmable transformation, Sci Adv, 8 eabn5460. DOI: https://doi.org/10.1126/sciadv.abn5460.

[58] Zhang Q, Zhang K, Hu G. Tunable fluid-solid metamaterials for manipulation of elastic wave propagation in broad frequency range. Appl Phys Lett 2018;112:221906. https://doi.org/10.1063/1.5023307.

[59] Wu L, Li Y. Harnessing bulging or sloshing modes to design locally resonant liquid-solid metamaterials. J Sound Vib 2021;510:116280. https://doi.org/10.1016/j.jsv.2021.116280.

[60] Yuan W, Chai Y, Yang X, Li Y. Bandgap evolution of metamaterials with continuous solid–liquid phase change. J Phys D Appl Phys 2023;56:055105. https://doi.org/10.1088/1361-6463/acaed8.

[61] Wang T, Cui H, Dong W, Wang Y, Xie K, Chen M. Vibroacoustic characteristics of a metamaterial plate cavity coupling system. Appl Acoust 2025;235:110685. https://doi.org/10.1016/j.apacoust.2025.110685.

[62] Li Y, Liu Z, Zhou H, Yi K, Zhu R. Broadening bandgaps in a multi-resonant piezoelectric metamaterial plate via bandgap merging phenomena. Sci Rep 2024;14:16127. https://doi.org/10.1038/s41598-024-66849-6.

[63] Yi K, Collet M. Broadening low-frequency bandgaps in locally resonant piezoelectric metamaterials by negative capacitance. J Sound Vib 2021;493:115837. https://doi.org/10.1016/j.jsv.2020.115837.

[64] Airoldi L, Ruzzene M. Design of tunable acoustic metamaterials through periodic arrays of resonant shunted piezos. New J Phys 2011;13:113010. https://doi.org/10.1088/1367-2630/13/11/113010.

[65] Lv W, Li D, Ren X. A self-recoverable negative stiffness metamaterial with enhanced bearing and energy dissipation capacity. Smart Mater Struct 2024;33:025035. https://doi.org/10.1088/1361-665X/ad1e8e.

[66] Jiang T, Han Q, Li C. Design and compression-induced bandgap evolution of novel polygonal negative stiffness metamaterials. Int J Mech Sci 2024;261:108658. https://doi.org/10.1016/j.ijmecsci.2023.108658.

[67] Goldsberry BM, Haberman MR. Negative stiffness honeycombs as tunable elastic metamaterials. J Appl Phys 2018;123:091711. https://doi.org/10.1063/1.5011400.

[68] Hu G, Tang L, Xu J, Lan C, Das R. Metamaterial with local resonators coupled by negative stiffness springs for enhanced vibration suppression. J Appl Mech 2019;86. https://doi.org/10.1115/1.4043827.

[69] Hewage TAM, Alderson KL, Alderson A, Scarpa F. Double-negative mechanical metamaterials displaying simultaneous negative stiffness and negative poisson's ratio properties. Adv Mater 2016;28:10323–32. https://doi.org/10.1002/adma.201603959.

[70] Zhang K, Qi L, Zhao P, Zhao C, Deng Z. Buckling induced negative stiffness mechanical metamaterial for bandgap tuning. Compos Struct 2023;304:116421. https://doi.org/10.1016/j.compstruct.2022.116421.

[71] Chronopoulos D, Antoniadis I, Ampatzidis T. Enhanced acoustic insulation properties of composite metamaterials having embedded negative stiffness inclusions. Extreme Mech Lett 2017;12:48–54. https://doi.org/10.1016/j.eml.2016.10.012.

[72] J. Gardan, Smart materials in additive manufacturing: state of the art and trends, virtual and physical prototyping, 14 (2019) 1-18.DOI: https://doi.org/10.1080/17452759.2018.1518016.

[73] Shrestha P, Joshi B, Li X, Ramaswamy N, Wang J, Shan X, Mo YL. Development of MRE-based metamaterial with adjustable frequency bandgap for seismic vibration isolation. J Build Eng 2024;91:109575. https://doi.org/10.1016/j.jobe.2024.109575.

[74] An Z, Li Y, Luo X, Huang Y, Zhang R, Fang D. Multilaminate metastructure for high-temperature radar-infrared bi-stealth: topological optimization and near-room-temperature synthesis. Matter 2022;5:1937–52. https://doi.org/10.1016/j.matt.2022.04.011.

[75] Wang Y, Xing J, Chen Z, Zhu X, Huang J. Topology optimization of two-dimensional magnetorheological elastomer phononic crystal plate with tunable bandgap considering a specified target frequency. Optim Eng 2025;26:31–51. https://doi.org/10.1007/s11081-024-09889-1.

[76] Liu K, Han L, Hu W, Ji L, Zhu S, Wan Z, Yang X, Wei Y, Dai Z, Zhao Z, Li Z, Wang P, Tao R. 4D printed zero Poisson's ratio metamaterial with switching function of mechanical and vibration isolation performance. Mater Des 2020;196:109153. https://doi.org/10.1016/j.matdes.2020.109153.

[77] Wang Q, Chen Z, Wang Y, Gong N, Yang J, Li W, Sun S. A metamaterial isolator with tunable low frequency stop-band based on magnetorheological elastomer and magnet spring. Mech Syst Signal Process 2024;208:111029. https://doi.org/10.1016/j.ymssp.2023.111029.

[78] C. Lou, B. Liu, X. Cao, L. Gao, S. Xuan, H. Deng, X. Gong, Dual-modulus 3D printing technology for magnetorheological metamaterials-part II: negative regulation theory and application, Compos A: Appl Sci Manuf, 177 (2024) 107893.DOI: https://doi.org/10.1016/j.compositesa.2023.107893.

[79] Zou B, Liang Z, Zhong D, Cui Z, Xiao K, Shao S, Ju J. Magneto-thermomechanically reprogrammable mechanical metamaterials. Adv Mater 2023;35:2207349. https://doi.org/10.1002/adma.202207349.

[80] Li L, Yao H, Mi S. Magnetically driven modular mechanical metamaterials with high programmability, reconfigurability, and multiple applications. ACS Appl Mater Interfaces 2023;15:3486–96. https://doi.org/10.1021/acsami.2c19679.

[81] Leanza S, Wu S, Sun X, Qi HJ, Zhao RR. Active materials for functional origami. Adv Mater 2024;36:2302066. https://doi.org/10.1002/adma.202302066.

[82] Behl M, Lendlein A. Shape-memory polymers. Mater Today 2007;10:20–8. https://doi.org/10.1016/S1369-7021(07)70047-0.

[83] Li B, Zhang C, Peng F, Wang W, Vogt BD, Tan KT. 4D printed shape memory metamaterial for vibration bandgap switching and active elastic-wave guiding. J Mater Chem C 2021;9:1164–73. https://doi.org/10.1039/D0TC04999A.

[84] Wei Y-L, Yang Q-S, Tao R. SMP-based chiral auxetic mechanical metamaterial with tunable bandgap function. Int J Mech Sci 2021;195:106267. https://doi.org/10.1016/j.ijmecsci.2021.106267.

[85] Yang H, Wang W-J, Zhu J-Z, Ma L, Pasini D, Zhai W. Temperature-driven topological transformations in prestressed cellular metamaterials. Adv Funct Mater 2025;35:2413962. https://doi.org/10.1002/adfm.202413962.

[86] Zeng C, Liu L, Hu Y, Zhao W, Xin X, Liu Y, Leng J. Stair-stepping mechanical metamaterials with programmable load plateaus. Adv Funct Mater 2024;34:2408887. https://doi.org/10.1002/adfm.202408887.